Nano Research

ISSN 1998-0124 CN 11-5974/O4
https://doi.org/10.26599/NR.2026.94908733

Research Article

Inter-protocellular macromolecular communication via nanoparticle-induced gap-junction mimics

Qixiao Guan[1,§], Jianwen Zhang[2,§], Yonghui Qian[1], Yaxin Cui[1], Shuo Yang[1], Ruoxu Gu[2](✉), Hongjing Dou[1](✉)

[1] The state Key Laboratory of Metal Matrix Composites, School of Materials Science and Engineering, Shanghai Jiao Tong University, Shanghai 200240, China

[2] School of Life Sciences and Biotechnology, Shanghai Jiao Tong University, Shanghai 200240, China

[§] Qixiao Guan and Jianwen Zhang contributed equally to this work.

Nano Res., **Just Accepted Manuscript** • https://doi.org/10.26599/NR.2026.94908733

https://www.sciopen.com/journal/1998-0124 on Apr. 10, 2026

Just Accepted

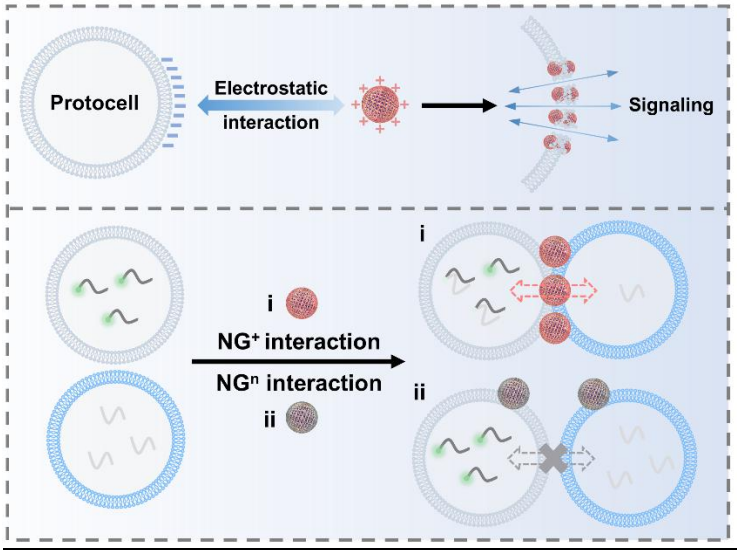

Gap-junction–like structures mediate cell–cell communication in multicellular organisms, yet mimicking these channels for macromolecular communication in protocells remains challenging. We constructed positively charged nanoparticles mediate protocell higher- order assembly via electrostatic attraction, inducing gap- junction- mimic nanochannels for directional inter- protocellular signaling and macromolecular communication.

Nano Research

Open Access

Research Article

Inter-protocellular macromolecular communication via nanoparticle-induced gap-junction mimics

Qixiao Guan[1,§], Jianwen Zhang[2,§], Yonghui Qian[1], Yaxin Cui[1], Shuo Yang[1], Ruoxu Gu[2] ✉, and Hongjing Dou[1] ✉

[1] *The state Key Laboratory of Metal Matrix Composites, School of Materials Science and Engineering, Shanghai Jiao Tong University, Shanghai 200240, China*

[2] *School of Life Sciences and Biotechnology, Shanghai Jiao Tong University, Shanghai 200240, China*

[§] Qixiao Guan and Jianwen Zhang contributed equally to this work.

Received: 10 March 2026; **Revised:** 9 April 2026; **Accepted:** 10 April 2026

✉ Address correspondence to Ruoxu Gu, mircial@sjtu.edu.cn; Hongjing Dou, hjdou@sjtu.edu.cn

Cite this article: *Nano Research*, 2026, 19, 94908733 https://doi.org/10.26599/NR.2026.94908733

ABSTRACT: Multicellular organisms rely on cell-cell contacts and substance exchange via transmembrane channels such as gap-junctions to maintain their biological behavior. Despite substantial advances in protocell-environment signaling, key challenges persist in developing synthetic channels that mimic the natural gap-junctions for macromolecular transport in protocells. Here, we developed an electrostatic interaction-based strategy for constructing nanoparticle-mediated gap-junction mimics in the membrane of protocells, investigating electrostatic modulation of membrane integrity and subsequent transmembrane signaling regulation. By engineering interactions between charged nanoparticles and protocell membrane, we modulated the contact and higher-order assembly behavior of protocells. We also achieved molecular weight-dependent and concentration gradient-controlled directional transmembrane transport of macromolecular signals between protocells. Further integrating molecular dynamics simulations with experimental validation, we systematically deciphered nanoparticle-membrane interaction dynamics and established the mechanism of electrostatic regulation in transmembrane communication. In summary, this study offers promising insights into the physical principles underlying transmembrane signaling and establishes a foundation for constructing synthetic cellular networks with advanced macromolecular communication functionalities.

KEYWORDS: gap-junction mimics, protocells, macromolecular communication, charged nanoparticles, electrostatic interaction

Introduction

In multicellular organisms characterized by sophisticated biological systems, intimate cell-cell contact and intercellular signaling play indispensable roles in sustaining physiological homeostasis. The plasma membrane, while serving as an essential barrier that preserves cellular integrity by segregating intracellular and extracellular compartments, intrinsically restricts direct intercellular substance exchange, which has become a central target for breakthroughs in the field of artificial cell communication. Notably, biological systems have evolved an array of intercellular junction structures and transmembrane transport mechanisms that not only mediate cell-cell adhesion and organization, but also establish regulated membrane channels to potentiate intercellular exchange and signaling cascades. Among these channels, intercellular gap-junctions formed by connexin proteins serve a cardinal function by physically coupling adjacent cells, thereby enabling direct intercellular communication and facilitating the transmembrane flux of ions and small signaling molecules.[1] Furthermore, native nanostructures such as tunneling nanotubes and pannexins constitute crucial pathways for intercellular communication.[2, 3] Analogously, diverse membrane-active biomolecules, encompassing cell-penetrating peptides,[4-7] perforin,[8-10] and melittin,[11, 12] play pivotal roles in mediating transmembrane drug delivery and inducing pore formation. Consequently, elucidating the mechanisms governing intercellular gap-junctions and transmembrane communication carries profound scientific implications, both for deciphering membrane-associated pathophysiological mechanisms and for reconstituting artificial multicellular systems.

Giant unilamellar vesicles (GUV) provide a simplified yet powerful protocell platform for bottom-up construction of well-defined cellular communication systems, enabling precise engineering of synthetic signaling networks while avoiding native biological complexity.[13-17] Various biomolecular architectures, including DNA nanostructures, peptide complexes, and macromolecular assemblies, have been engineered to create functional transmembrane channels in protocell membranes, thereby facilitating intercompartmental molecular transport and signal transduction.[18-21] DNA nanostructures, with their tunable properties, have been employed to integrate into membranes,[22, 23] remodel synthetic cell membranes with membrane channel formation,[24] and regulate cellular communication behaviors in artificial and living cells.[25-29]

Similarly, engineered peptide complexes and macromolecular assemblies form functional nanopores that construct artificial membrane channels,[10, 11, 30-32] while mimicking biological ion-gating behavior to enable responsive signaling.[33-35] Additionally, chemically structured nanopores utilize hydrophobic/hydrophilic interactions to enhance ion transport,[36, 37] while precision-engineered artificial gap-junction channels concurrently facilitate intercellular signal coupling and small molecule exchange,[38] thus collectively advancing synthetic cell communication engineering. However, current protocell signaling efforts primarily focus on individual protocell-environment interactions, whereas contact-dependent communication offers superior precision and efficiency.[19, 39-41] Moreover, the fundamental properties of gap-junction-mimic channels (e.g., surface charge, dimensions) and their effects on phospholipid membrane characteristics remain insufficiently explored in the context of inter-protocellular communication. Most critically, the existing systems remain limited to ionic/small-molecule exchange, with macromolecular transport through synthetic gap-junction analogs representing a major unmet challenge for advancing the field.

Through the prior investigations of the mechanisms underlying intercellular communication networks, we identified electrostatic interactions as a critical factor of both cell-cell contact/assembly and gap-junction-mediated transmembrane signaling.[1, 22, 42-48] These electrostatic effects also play a significant role in regulating the performance of the aforementioned nanopores, directly impacting the mechanisms and efficiency of ion and signaling molecule transport.[23, 38, 49] Although the applications of nanoparticles in lipid-vesicle regulation have been investigated,[50-52] their integration with synthetic inter-protocellular communication systems has yet to be established. Inspired by these insights, we herein developed an electrostatics-assisted strategy to facilitate nanoparticle-mediated protocell assembly with gap-junction-mimic interfaces, thus enabling regulated intercellular molecular weight-directed macromolecular communication within adjacent protocell communities (Scheme 1). This approach allowed systematic investigation of protocell contact dynamics and higher-order assembly along with inter-protocellular communication, thus providing insights into their regulatory effects on phospholipid membrane. Such membrane modulation and perturbation may potentially induce the formation of membrane channels,[53-55] ultimately facilitating the emergence of macromolecular signaling interfaces within protocell communities. Concurrently, molecular dynamics simulations revealed nanoparticle-membrane interaction patterns and the mechanistic role of electrostatic forces in membrane regulation. Our study conclusively demonstrated that the synergistic combination of electrostatic interactions and nanoparticle assembly can establish gap-junction-like signaling conduits capable of facilitating macromolecular-scale communication, thereby establishing a programmable platform for engineering spatially organized protocellular networks with designed signaling capabilities.

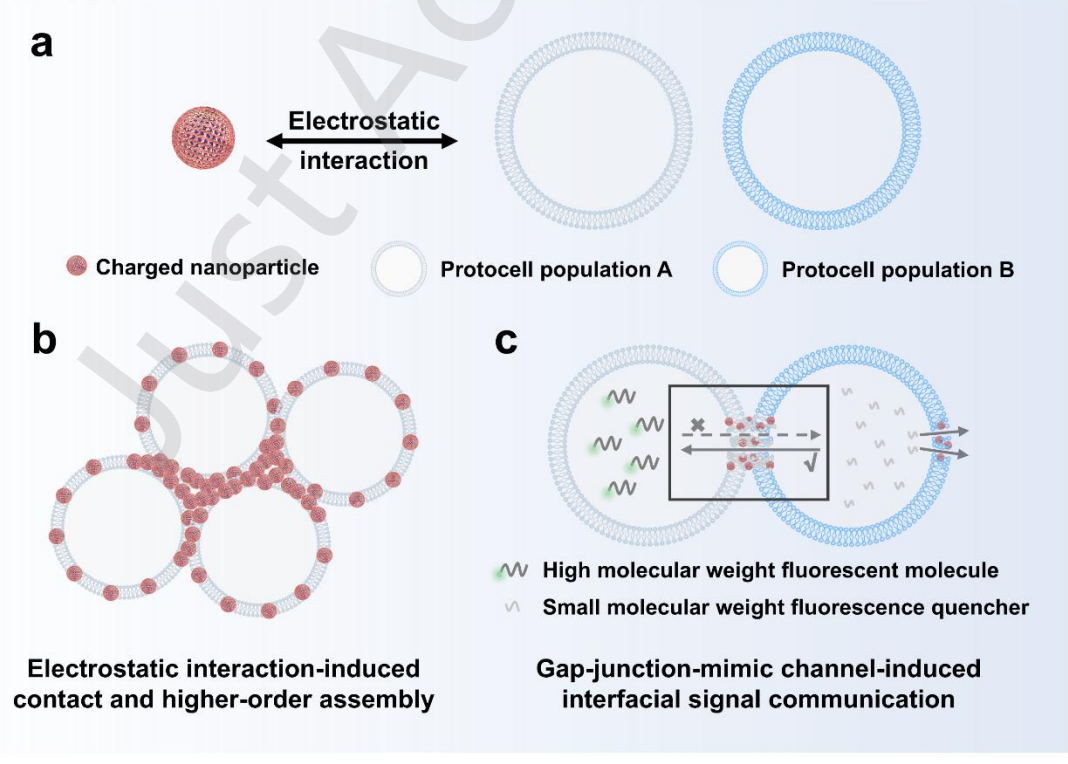

Scheme 1. Schematic illustration of positively charged nanoparticle-mediated higher-order assembly of protocells and the consequent formation of gap-junction-mimic channels enabling directional inter-protocellular signal communication. a) Electrostatically mediated interactions between charged nanoparticles and protocell populations. b) Electrostatic interaction directed protocell contact-assembly. Electrostatic attraction between charged nanoparticles and the protocell membrane with counterpart charge first drives surface contact and adhesion, enabling higher-order assembly of protocells. c) The positively

charged nanoparticles induce nanochannel formation in protocell membranes, facilitating bidirectional transmembrane communication of molecular cargo and signaling mediators at the interfacial region. Within the electrostatically enriched zones at membrane-membrane interfaces between protocells, positively charged nanoparticles facilitate the assembly of bioinspired junctional nanochannels, structurally and functionally analogous to biological gap-junctions, thereby enabling inter-protocellular signal communication.

Results and Discussion

1. Electrostatically anchored positively charged nanoparticles drive protocell adhesion and assembly.

To investigate interfacial effects mediated by electrostatic attraction in nanoparticle-protocell interactions, we engineered positively charged polysaccharide nanogel particles (NG^+) through quaternary ammonium functionalization (Figure S1), building upon our previous work to confer strong cationic character.[47, 56-58] Briefly, we implemented a graft copolymerization-induced self-assembly (GISA) strategy by conducting graft copolymerization of hydrophobic chains on polysaccharide backbones to construct polysaccharide nanogel particles (NGs) via subsequent self-assembly, while utilizing the facile modifiability of polysaccharide structures to introduce quaternary ammonium groups for imparting positive charge characteristics. Notably, unlike solid nanoparticles (e.g., gold nanoparticles), NG^+ exhibits amphiphilic properties during its self-assembly. This structural similarity to phospholipids is expected to drive unique interfacial behaviors in lipid-based protocell systems. In parallel, giant unilamellar vesicles (GUVs) serve as optimal protocell models that faithfully replicate native cell membrane composition and architecture while avoiding interference from the complex physicochemical properties of living cells. To simultaneously emulate both the composition and anionic characteristic of natural cell membranes, we employed the electroformation method[59-62] to construct a stable foundational protocell model (GUV^n) using POPC (1-Palmitoyl-2-oleoyl-sn-glycero-3-PC) and cholesterol as primary components, wherein POPC phospholipid represents a physiologically abundant amphiphilic lipid containing negatively charged phosphate groups and positively charged choline moieties. In aqueous environments, hydrophobic interactions induce choline group burial and phosphate group exposure at the membrane surface, thus conferring a net negative surface charge to GUV^n.[63, 64] Consequently, NG^+ exhibit distinct interaction profiles with protocells compared to their uncharged counterparts (Figure 1a).

Zeta potential characterization of the nanoparticles (Figure 1b) revealed a significant gradient between NG^+ and its neutral control nanoparticle NG^n, showing a pronounced contrast with the zeta potential of the protocell model GUV^n (Figure S2). Morphological characterization (Figure 1c, Figure S3) revealed monodisperse nanoscale spherical structures, thus demonstrating a distinct size hierarchy with the micrometer-scale GUV^n protocells (Figure S2). This precisely engineered scale disparity enables nanoscale interfacial control over protocell behavioral regulation and inter-protocellular communication. To visualize these interactions, we equivalently labeled the NGs with Cy5.5 (exhibiting red fluorescence; Figure S3d) and GUV^n protocells with DiO (exhibiting green fluorescence; Figure S2b), thus facilitating confocal laser scanning microscopy (CLSM) analysis of their spatial distribution and interaction patterns.

Following incubation with protocells, NG^+ and NG^n exhibited fundamentally distinct interaction patterns, as demonstrated in Figure 1d. NG^+ displayed pronounced membrane-anchoring characteristics with predominant peripheral localization at lipid bilayer interfaces, suggesting that strong electrostatic adsorption had taken place. In contrast, NG^n appeared inside the protocells, and was presumably internalized through phospholipid translocation mediated by its nanoscale high surface energy. This phenomenon was further corroborated by the line profiles in Figure 1e, which showed Cy5.5 fluorescence (representing NG^n) and DiO fluorescence (representing phospholipids) within the protocell membrane. Furthermore, while the NG^n→Protocell group maintained an intact protocell morphology, the NG^+→Protocell group exhibited emerging tight contacts and progressive interconnections leading to assembly, as visually confirmed by the 3D reconstruction images in Figure S4.

To further elucidate the dynamic regulatory mechanisms underlying NG^+-protocell interactions, we established a comprehensive temporal framework to precisely characterize their evolving binding modalities. Time-dependent co-incubation experiments (Figure S5) revealed a distinct hierarchical assembly pathway mediated by electrostatic interactions. NG^+ initially established stable membrane anchoring via electrostatic attraction, and subsequently exerted effects on the external environment at around 2 h to induce tight contact and connection between protocells, and ultimately facilitated higher-order protocell assembly beyond 4 h. Through fixed-position observations at finer time intervals (Figure 1f), we observed that NG^+ indeed progressively intensifies its interaction with protocells, inducing protocell immobilization and membrane deformation to achieve higher-level interconnections. In stark contrast, NG^n-treated protocells maintained motile freedom and structural integrity throughout the 100-min observation period. Furthermore, to investigate the modulation of NG^+ amount on its mediated local membrane deformation, we added a doubled concentration of NG^+, resulting in the observation of more intensive and rapid interaction-induced protocell deformability and assembly characteristics (Figure S6). Similar to the aforementioned observations at fine time intervals, the membrane mobility decreased after deformation, producing a protocell immobilization effect. This also validates the primary influence of electrostatic interaction strength on the interaction between NG^+ and protocells.

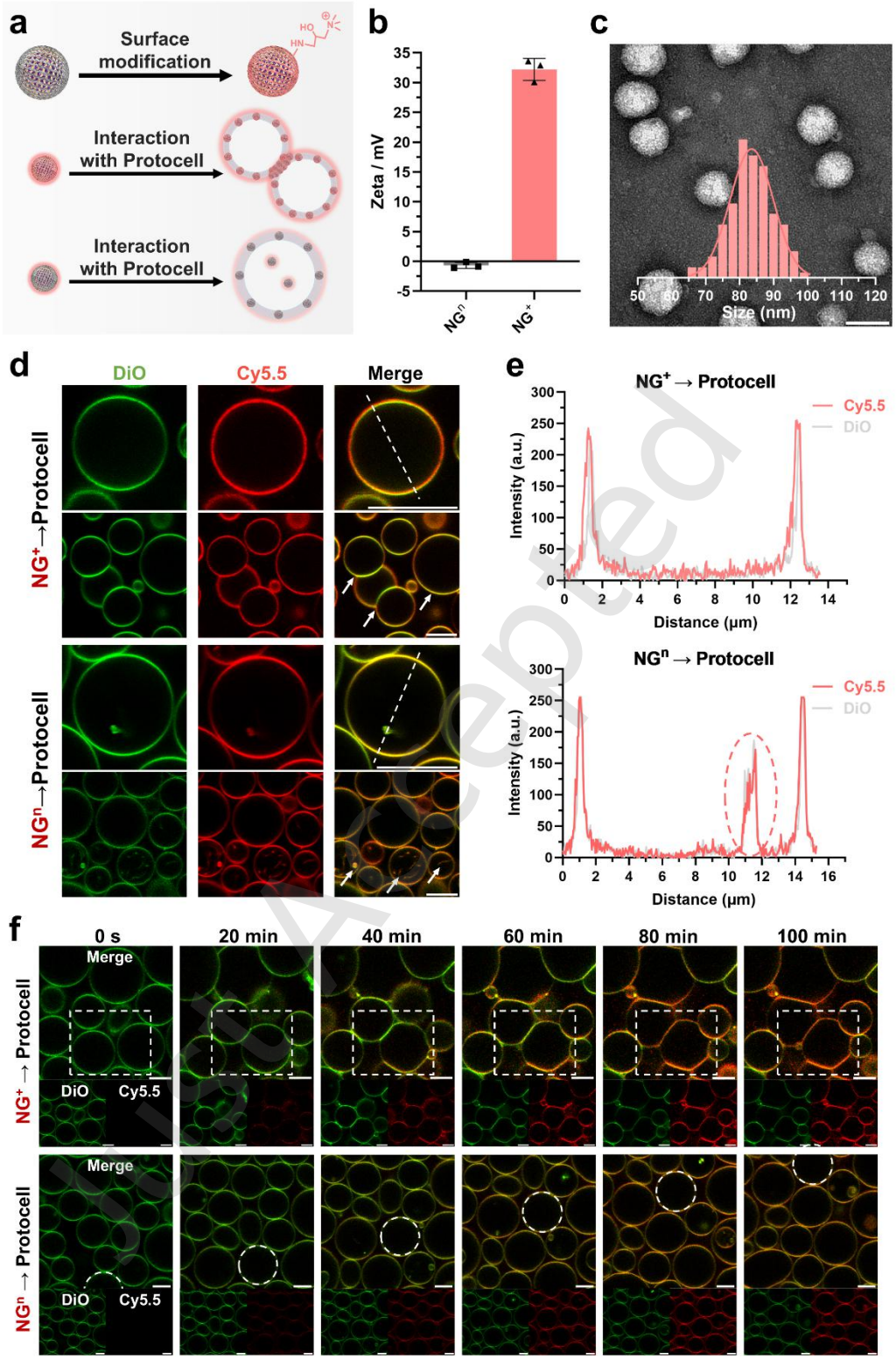

Figure 1. Electrostatic potential-driven enrichment and membrane anchoring of NG^+ on protocells, mediating the progressive stages of protocell interaction: from initial contact to stable adhesion and eventual higher-order assembly. a) Schematic illustration depicting the fabrication of NG^+ and their differential interaction profiles with protocells compared to uncharged nanoparticles. b) Zeta potentials of NG^n and NG^+. Data were presented as the mean ± standard deviation (SD, n = 3). c) TEM image and the diameter of NG^+ calculated from TEM images. Scale bar: 100 nm. d) Confocal microscopy images of protocells after 2 h co-incubation with NG^+ and NG^n, revealing two distinct interaction modalities: i) membrane accumulation of NG^+, and induced inter-protocell contact, ii) transmembrane entry of NG^n, as indicated by the white arrows. Scale bar: 10 μm. e) Line profiles along white dashed lines in d). f) Confocal microscopy images of protocells co-incubated with NG^+ and NG^n for 20, 40, 60, 80, and 100 min, respectively, highlighting the anchoring properties of NG^+ on the protocells and the enhanced membrane interactions.

2. Validation of NG^+-mediated membrane anchoring and gap-junction-mimic channel induction.

Subsequently, we systematically validated the membrane-anchoring properties of NG^+, with a particular focus on its interfacial interactions with protocell phospholipid membranes, and further explored its potential for mediating transmembrane communication. Initial quantitative analysis of intra-protocellular fluorescence intensity using ImageJ revealed that NG^n exhibited significantly higher fluorescence intensity within protocells compared to NG^+ after 2 hours of interaction (Figure 2a). However, flow cytometry measurements with mean fluorescence intensity (MFI) quantification (Figure 2b,c) demonstrated higher whole fluorescence intensity of the NG^+ group, validating its stronger binding affinity with protocells. The combined interpretation of these results highlights the distinct membrane localization characteristics of NG^+ compared to NG^n, confirming the superior membrane accumulation of NG^+, and providing direct evidence for electrostatic attraction-enhanced surface binding.

We next corroborated NG^+'s membrane-anchoring signature with a fluorescence-quenching assay. We conjugated NGs with the quencher molecule BHQ1 to produce QNG^n and QNG^+, both of which retained their original physicochemical properties (e.g., size and zeta potential) following the post-modification process, to achieve successful functionalization of nanoparticles with fluorescence without affecting their particle size and surface (Figure S7). These QNGs were incubated with protocells that had been internally loaded with FITC-Dextran ($FGUV^n$) to monitor intra-protocell fluorescence quenching (Figure 2d). Confocal microscopy images (Figure 2e) demonstrated pronounced fluorescence quenching in the QNG^n group due to its transmembrane translocation, whereas the QNG^+ group exhibited negligible fluorescence reduction while preserving its assembly-inducing capability. The results of the quantitative analysis performed with ImageJ on the differential FITC fluorescence intensity inside the $FGUV^n$ protocells before and after the addition of QNG^n and QNG^+ also confirmed this finding (Figure S8). Additionally, in the QNG^+ group, the homogeneous fluorescence distribution across QNG^+-induced protocell-assemblies indicated efficient inter-protocell signaling homogenization and communication. These findings were further corroborated by flow cytometry and MFI analysis (Figure 2f,g), which quantitatively verified NG^+'s exclusive membrane localization and functional persistence.

Having confirmed NG^+'s membrane-anchoring capability and protocell assembly induction, we further investigated the pivotal role of electrostatic attraction by engineering charge-polarized protocell models (GUV^+/GUV^-) incorporating permanently cationic (DOTAP, 2,3-Dioleoyloxy-propyl-trimethyl-ammonium-chloride) and anionic (DOPA, 1,2-Dioleoyl-sn-glycero-3-phosphoric acid) lipids (Figure S9). All three models (GUV^-, GUV^n, GUV^+) displayed uniform spherical morphologies with comparable diameters (~15 μm; GUV^+ slightly smaller at ~10 μm), maintaining a consistent size disparity with the nanoparticles. Correspondingly, we synthesized negatively charged NG^- (zeta potential confirmed in Figure S3c). Co-incubation of charge-complementary pairs (NG^+/GUV^- group and NG^-/GUV^+ group) for 2 h effectively promoted protocell contact, bridging, and assembly (Figure 2j). While multiple interaction forces exist between nanoparticles and phospholipid membranes,[65] our results conclusively establish electrostatic interactions as the predominant mechanism in the present system. This protocell deformation is driven by electrostatic-mediated nanoparticle adsorption and subsequent membrane stress accumulation. Electrostatic attraction between oppositely charged nanoparticles and lipid membranes promotes rapid nanoparticle binding, and as more nanoparticles accumulate, the locally induced surface charge imbalance generates tensile stress on the lipid bilayer, disrupting the spontaneous curvature equilibrium of the membrane. Subsequently, the accumulated surface stress and spatial interactions induce membrane remodeling, leading to the observed morphological changes and nanoparticle-membrane assembly.

To directly visualize NG^+-membrane interfacial interactions while circumventing their size disparity, we constructed nanoscale protocells (nano-protocells) with identical phospholipid composition for high-resolution cryogenic transmission electron microscopy (cryo-TEM) imaging. As evidenced in Figure 2k and Figure S10, both cryo-TEM and TEM images revealed NG^+ enrichment, anchoring, and even partial embedding at nano-protocell membranes. Strikingly, cryo-TEM further resolved NG^+ functioning as inter-protocell hinges between adjacent nano-protocells, providing structural visualization of its electrostatic bridging mechanism underlying macroscale assembly.

Remarkably, our observations of NG^+-nano-protocell interactions suggested potential localized membrane perturbations and phospholipid rearrangement that may facilitate transmembrane exchange of typically membrane-restricted molecules/signals. This hypothesis was validated through dye leakage assays (Figure 2h), which revealed significantly enhanced fluorescence intensity in NG^+-treated nano-protocells. This increase indicates that both encapsulated fluorophores and their corresponding quenchers escaped through NG^+-perturbed regions, thereby exceeding the Förster quenching distance.[66] These findings not only establish the capacity of NG^+ to cluster protocells, but also reveal its profound membrane-remodeling effects, likely through formation of gap-junction-mimic channels, to mediate transmembrane signaling (Figure 2i).

Building upon these findings, we engineered protocells that were externally loaded with FITC-Dextran ($WFGUV^n$) of varying molecular weights (Figure S11), where differential permeability patterns following NG^+ treatment provided indirect characterization of membrane-embedded nanochannels. As demonstrated in Figure 2l, FITC-Dextran with molecular weights below 10 kDa readily permeated into protocell interiors through NG^+-induced gap-junction-mimic channels. This permeability was significantly enhanced in pre-assembled protocell clusters, indicating a positive correlation between NG^+-mediated surface enrichment, assembly induction, and nanochannel formation.

In contrast, 10 kDa FITC-Dextran exhibited no detectable intracellular signal, even within interconnected protocell networks, thus establishing that NG^+-generated nanochannels maintain a strict size exclusion limit between 4-10 kDa. These molecular weight size-selective transport properties enable directional transmembrane communication while maintaining protocell integrity.

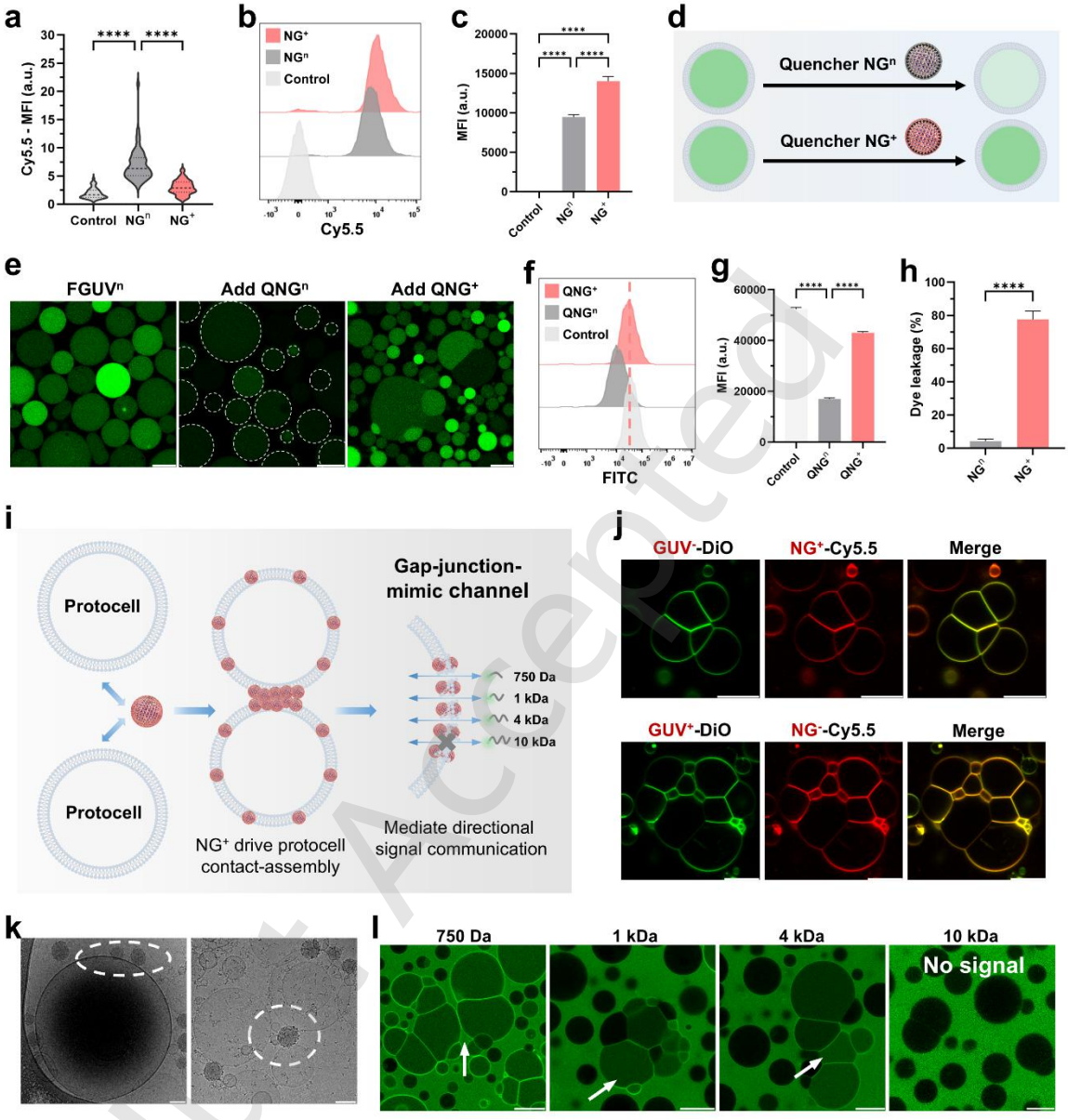

Figure 2. Verifying the membrane anchoring property of NG^+ and the electrostatic-driven protocell assembly, and demonstrating the NG^+-induced nanochannel formation for bidirectional transmembrane communication. a) Statistical analysis of mean fluorescence intensity of Cy5.5 within protocells following 2 h interaction between NGs and GUV^n. Data were presented as violin plots displaying kernel density distributions, showing median (central dot) and interquartile range (inner whiskers), n = 50. b) Flow cytometry data and c) quantified analysis of MFI for GUV^n that had been incubated with NG^n and NG^+, respectively. d) Schematic illustration of fluorescence quenching process induced by transmembrane translocation of the Quencher NG^n into FITC-dextran-loaded protocell ($FGUV^n$), while Quencher NG^+ does not cause fluorescence quenching inside the protocell due to its membrane anchoring property. e) Confocal microscopy images acquired after 2 h co-incubation of Quencher NGs with $FGUV^n$ composed of FITC-Dextran, demonstrated significant differences in fluorescence reduction. Scale bar: 10 μm. f) Flow cytometry data and g) quantified analysis of MFI for $FGUV^n$ that had been incubated with Quencher NGs. Data were presented as the mean ± standard deviation (SD, n = 3). h) Dye leakage from nano-protocells incubated with NG^n or NG^+ for 30 min. i) Schematic illustration demonstrating that NG^+ facilitates protocell contact-assembly through electrostatic interactions and induces the formation of gap-junction-mimic channels on membranes to mediate directional signal communication. j) Confocal microscopy images of charge-complementary protocell-nanoparticle pairs (i.e., $NG^+ \rightarrow GUV^-$ group, $NG^- \rightarrow GUV^+$ group) after 2 h of co-incubation. Scale bar: 10 μm. k) Cryo-TEM images of nano-protocells co-incubated with NG^+. Scale bar: 100 nm. l) Confocal microscopy images acquired after 2 h co-incubation of NG^+ with $WFGUV^n$ composed of FITC-Dextran with varying molecular weights, thus revealing the molecular size threshold for nanochannel-induced transmembrane signal transduction. Scale bar: 10 μm.

3. Integrated micro-macro analyses elucidate NG^+-induced membrane modulation and protocell communication mechanisms.

Based on the identified nanochannel potential, understanding the fundamental interactions between NG^+ and protocell membranes, particularly their structural and biophysical transformations, becomes crucial for advancing NG^+-mediated protocell regulation and transmembrane communication. We therefore conducted a multiscale investigation of NG^+-induced phospholipid membrane alterations through electrostatic interactions. Initially, angular dependent fluorescence anisotropy analysis revealed that NG^+ caused membrane perturbations, lipid disordering, and molecular reorientation. Specifically, in native membrane structures, the ordered arrangement of phospholipids produces photoselection effects where fluorophores with transition moments aligned parallel to the excitation polarization are preferentially excited.[67-69] Consequently, the relative orientation of fluorescent molecules to the excitation polarization plane generates measurable variations in emission intensity with observation angle (Figure S12). Similar effects were observed for uniformly distributed NG^n on membrane surfaces (Figure 3a, Figure S13). In contrast, the NG^+ exhibited significantly stronger and more complex interactions with the negatively charged membrane, involving intricate entanglement and interweaving with phospholipid molecules, thus leading to non-uniform surface distribution, disordered orientation, and localized microscopic aggregation. This structural disruption randomized fluorophore excitation, resulting in angle-independent fluorescence intensity and complete absence of polarization effects (Figure 3b, Figure S13). The angular fluorescence dependence thus provides compelling evidence for the strong interaction between NG^+ and the phospholipid membrane.

On the other hand, the changes in protocell membrane fluidity directly reflect the interaction strength between NGs and the phospholipid membrane, and the effect of NG^+ on membrane fluidity further supports its role in inducing nanochannel formation. Fluorescence recovery after photobleaching (FRAP) analysis of Cy5.5-labeled NGs and DiO-labeled membranes revealed that compared to the baseline fluidity of control GUV^n membranes (Figure S9), the addition of NG^n caused no significant change in fluidity (Figure 3c, Figure S14a), as observed for both membrane-associated DiO and nanoparticle-bound Cy5.5 fluorescence. While for the NG^+ group, both Cy5.5 and DiO exhibited markedly reduced fluorescence recovery rates and extents (Figure 3d, Figure S14b), indicating a coupled decrease in mobility between NG^+ and the phospholipid membrane. These results demonstrate the synchronized behavior of NG^+ and membrane phospholipids, confirming their strong interaction. Complementary fluorescence polarization anisotropy measurements that were performed using the membrane-embedded DPH (1,6-diphenyl-1,3,5-hexatriene) probe[70-72] provided further validation. Since increased anisotropy reflects restricted motion of the phospholipid acyl chains within the membrane, the elevated DPH polarization values (Figure 3h,i) directly demonstrate lower membrane fluidity, thus confirming NG^+-induced membrane rigidification, and corroborating the robust interaction between NG^+ and the phospholipid membrane.

Further investigation into the membrane tension of protocells revealed the existence of more profound intermolecular interactions induced by NG^+ on phospholipid membranes. The membrane tension can be quantitatively assessed by inserting a Flipper-TR membrane tension probe into the phospholipid bilayer of the protocell membrane and measuring its fluorescence lifetime.[73-75] Fluorescence lifetime imaging of protocell membranes (Figure 3e) and quantitative analysis of the fitted values (Figure 3f) clearly demonstrated that NG^+ treatment significantly reduced membrane tension compared to both untreated controls and NG^n-treated groups. This finding may contradict conventional expectations, as the incorporation of NG^+ unexpectedly reduced membrane tension. However, our theoretical framework provides a rational explanation and establishes the foundational principles for subsequent gap-junction-mimic nanochannel formation. Upon contact with the phospholipid membrane, NG^+ engages in strong electrostatic interactions with phospholipid molecules, thus inducing molecular disordering and entanglement with NG^+. This leads to the formation of localized high-density phospholipid packing around NG^+, thereby creating short-range phospholipid aggregates. From a macroscopic perspective, given a constant total phospholipid content, such short-range aggregation necessarily results in long-range loosening of the membrane structure. Consequently, the regions adjacent to NG^+'s position exhibit more relaxed phospholipid arrangements, collectively contributing to an overall reduction in membrane tension (Figure 3g). Correspondingly, as can be contrastively observed from the fluorescence lifetime imaging of the original protocells (Figure S15), the NG^+ treated vesicles interconnected and extended to occupy the entire field of view, with the expansion of total surface area corroborating the long-range loosening of the phospholipid membrane, leading to a reduction in overall membrane tension. The similar decrease in membrane tension observed when NG^+ interacted with strongly negatively charged GUV^- protocells (Figure S16) further corroborated the critical role of electrostatic interactions in this process. As a result, this structural characteristic of short-range aggregation and long-range loosening, combined with natural and appropriate molecular rearrangements, creates favorable conditions for the potential formation of nanoscale channels.

Finally, from a macroscopic perspective, we examined the mechanical properties of protocells before and after NGs addition (Figure S17), and quantitatively analyzed their Young's modulus (Figure 3j) to validate changes in macroscopic mechanical parameters. The results demonstrated that NG^+ significantly increased the protocell modulus, which is intrinsically associated with electrostatic interactions between NG^+ and the negatively charged membrane. This NG^+-induced solidification-like effect corroborates our previous confocal microscopy observations, further confirming the strong NG^+-protocell interaction

while illustrating NG^+'s capability to modulate overall protocell properties. The influence on the mechanical properties of protocells also exhibits significant connections with intercellular biochemical signal transduction, as previously explored in our earlier study,[76] and may relate to nanochannel formation at the protocell membrane interface. Taken together, these findings elucidate the fundamental mechanisms by which NG^+ facilitates protocell contact, assembly, and transmembrane nanochannel formation, while revealing its critical impact on phospholipid membrane organization.

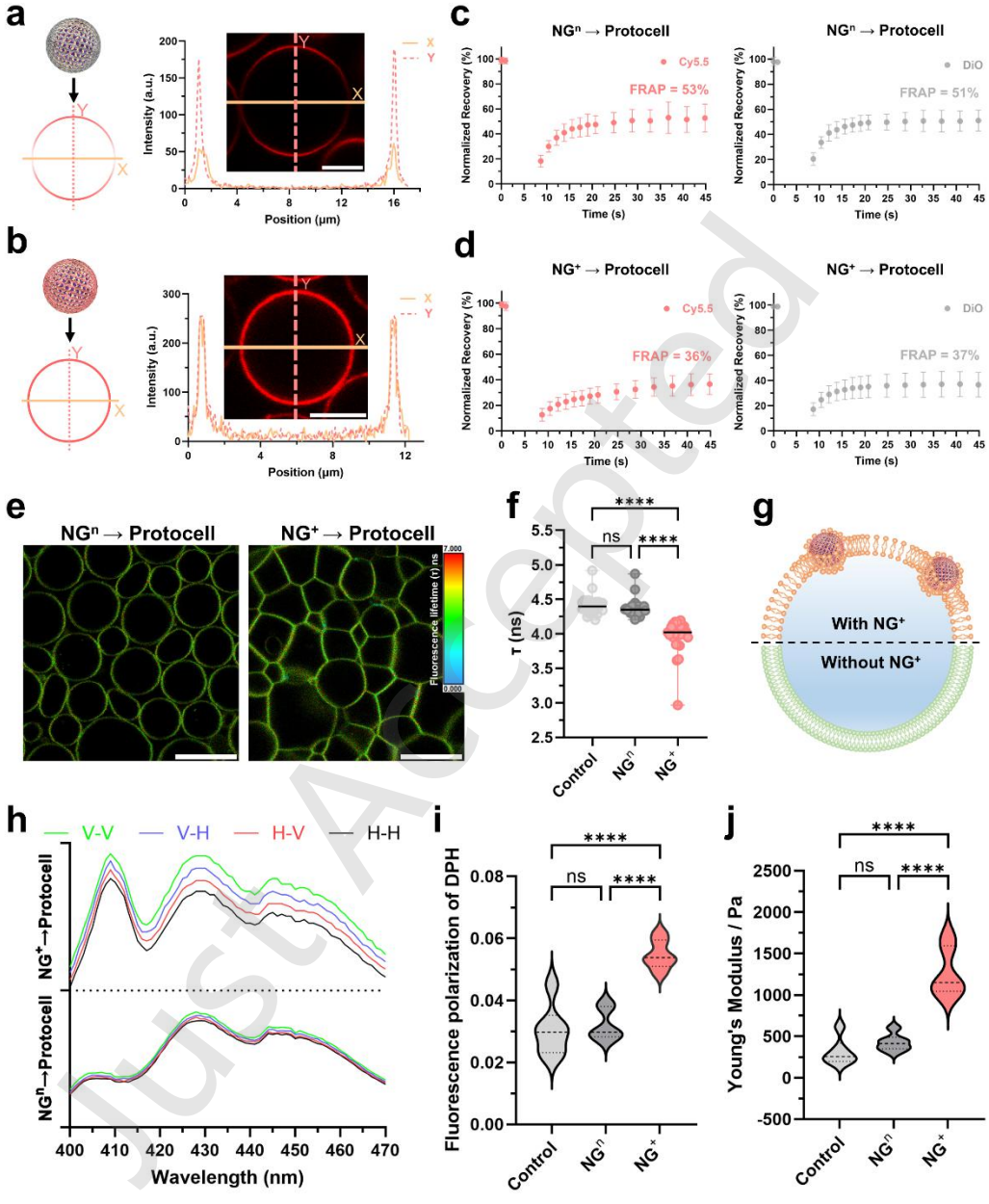

Figure 3. Systematic micro- and macro-scale analysis reveals the pronounced impacts of NG^+ on protocell phospholipid membranes, and elucidates their mechanistic role in facilitating transmembrane signal communication in protocell systems. a) Angular dependence of fluorescence of the NGs functionalized with Cy5.5 on protocell membranes. Polarization effect exhibited as a strong angular dependence of the intensity of NG^n functionalized with Cy5.5 along the protocell membrane, as emphasized with the line profiles along the respective solid or dashed lines indicated on the confocal microscopy image. Scale bar: 5μm. b) No polarization effect was observed on the protocell membrane after co-incubation with NG^+ functionalized with Cy5.5. The intensity line profiles were generated in the vertical and horizontal directions. Scale bars: 5 μm. c) FRAP data for nanoparticle fluorescence Cy5.5 and membrane fluorescence DiO in the NG^n→Protocell group, with fluorescence recovery rates of 53±6% and 51±4%. d) FRAP data for nanoparticle fluorescence Cy5.5 and membrane fluorescence DiO in the NG^+→Protocell group, with fluorescence recovery rates of 36±3% and 37±4%. Data are presented as the mean ± standard deviation (SD, n = 10). e) Fluorescence lifetime (τ) imaging of Flipper-TR probe in protocell after interaction with NG^n and NG^+. Scale bar: 20 μm. f) Statistical graphs showing individual data points indicating fluorescence lifetime τ of 30 selected regions-of-interest (ROIs) across three replicates. A double exponential fit was applied to the fluorescence decay. g) Schematic illustration highlighting the comparative effects of NG^+ incorporation on POPC phospholipid membrane structural reorganization and ordered phase modulation. h) Raw polarized fluorescence emission scans of the DPH probe in the

protocells of the NG^+ or NG^n groups. i) Calculated fluorescence polarization value of the DPH probe in protocell before and after interaction with NGs. Data are presented as the mean ± standard deviation (SD, n = 6). j) The Young's modulus of untreated protocells and protocells treated with NGs was calculated by fitting the AFM mechanical force data with the Hertzian model. Data are presented as the mean ± standard deviation (SD, n = 6).

4. Molecular dynamics simulations shed light on the underlying mechanism of NG^+-membrane interactions

Following this, to dissect deeper mechanistic understanding of NG^+-phospholipid membrane interactions and validate potential explanations for their mediation of transmembrane signaling, we constructed coarse-grained models of the polymers, which were able to assemble into polysaccharide nanogel particles (NGs) spontaneously in equilibrium simulations (NG^+ and NG^n, see supporting information for details of the coarse-grained model, Figure S18, Figure 4a). We then performed molecular dynamics simulations to investigate the mechanism underlying their interactions with POPC:cholesterol bilayers at the molecular scale (Figure 4). Free energy calculations using the umbrella sampling method[77] revealed much higher bilayer affinity for NG^+ compared to NG^n (-8 v.s. +5 kJ/mol, Figure 4b), demonstrating NG^+'s enhanced contacting stability with the bilayer compared to NG^n and aligns well with the experimental observations (Figure 1d,f). Equilibrium simulations of systems containing 5 nanoparticles (either NG^+ or NG^n) and a POPC:cholesterol bilayer confirmed the above results, showing dramatically higher bilayer contact probability for NG^+ compared to NG^n (Figure 4c,d). In these equilibrium simulations, NG^n particles are separated from each other and only contact with the bilayer occasionally, while the NG^+ particles aggregate and are attached to the membrane surface in most of the simulation time (Figure 4c,d).

Furthermore, we quantified the effects of nanoparticle-bilayer interactions on the membrane properties in equilibrium simulations to shed light on the structural basis of NG^+ mediated material translocation across bilayers. Specifically, we compared the order parameters of NG^+-contacted and non-contacted POPC lipids in the NG^+ containing system. Our measurements revealed consistently lower order parameter (-Scd) values across all three coarse-grained bonds of the NG^+-contacted lipids compared to the non-contacted lipids, indicating significant disordering of lipid tails induced by NG^+-membrane interactions (Figure 4e). In addition, the NG^+-containing system exhibited globally reduced membrane lipid tail order parameters relative to the NG^n-containing system, which can be attributed to the enhanced contact probability of NG^+ with the POPC:cholesterol bilayer (Figure 4e). Moreover, NG^+'s disturbance on lipid headgroups is also significant. The 2D density maps clearly revealed that NG^+ particles induce lipid headgroup rearrangement, resulting in notable regions with sparse headgroup distributions where NG^+ contacts the lipids (Figure 4f, Figure S19a). Conversely, NG^n exhibits negligible effects on lipid headgroup organization (Figure 4f, Figure S19a). Finally, we calculated both the mean and Gaussian curvatures of the two bilayer leaflets to characterize the global membrane architecture resulting from exposure to NG^+ and NG^n nanoparticles (Figure 4g, Figure S19b). Interactions between NG^+ and the lipid bilayers led to deformation of the membrane surface, with measurable local concavities and convexities of the bilayers arising from direct contact and electrostatic interactions between the nanoparticles and the membrane. In contrast, membranes exposed to NG^n showed negligible changes in their curvature due to the absence of characteristic interactions.

The NG^+-mediated local membrane deformations, together with the perturbation of lipid tail order parameters and headgroup densities, indicated that multiple NG^+ are able to interact with the POPC:cholesterol bilayer extensively, thus changing the membrane properties and potentially generating nanostructures that would be capable of molecular communications across bilayers.

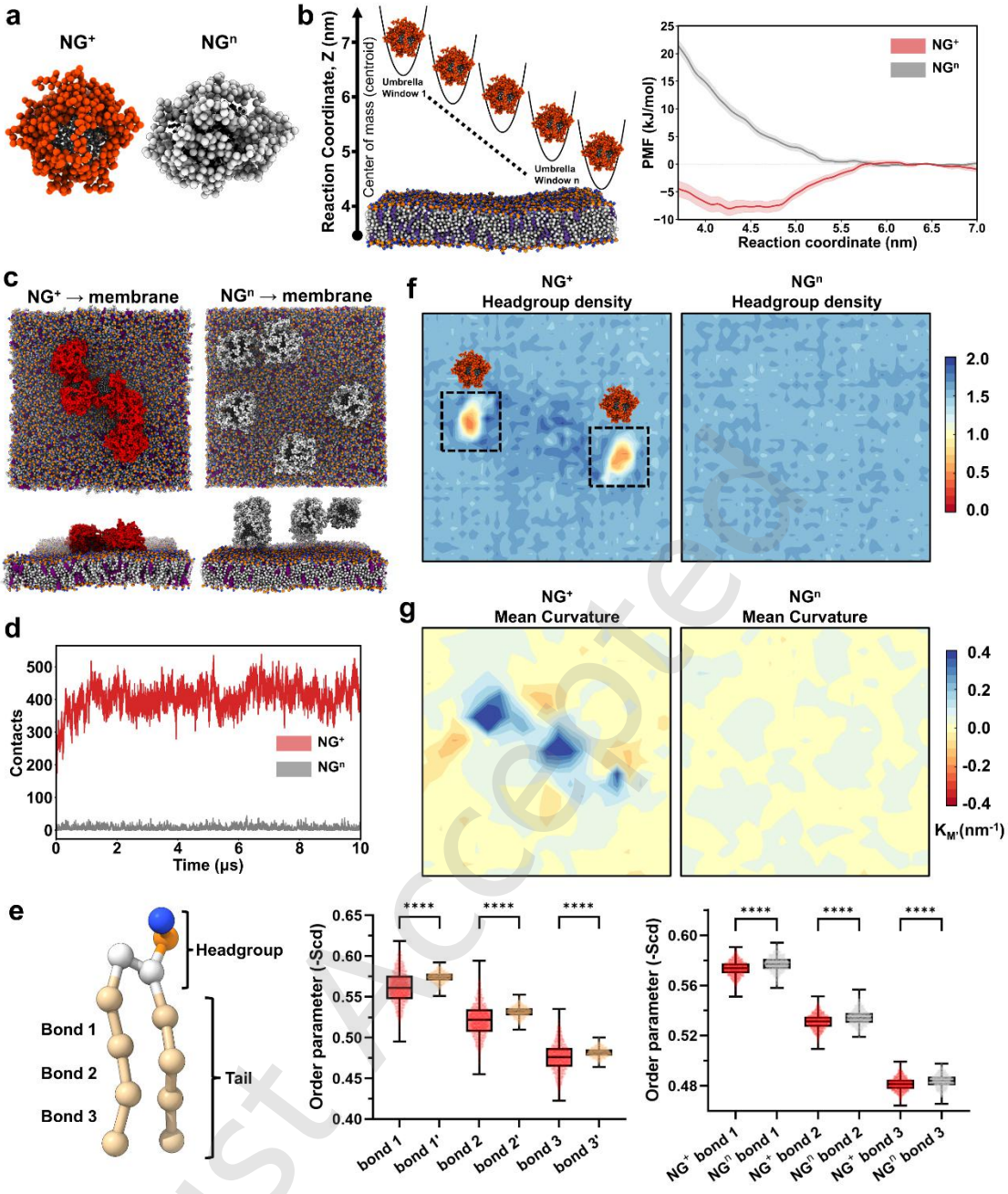

Figure 4. Molecular dynamics simulations shed light on the mechanism underlying nanoparticle-bilayer interactions. a) Coarse-grained models of the nanoparticles, with the polysaccharide chains of NG^+ and NG^n shown by sphere models in red and white. b) Free energy profiles of NG^+/NG^n approaching the membrane calculated by the umbrella sampling method. Left: distance between the centers of mass of NG^+/NG^n and the bilayer is used as the reaction coordinate. Right: free energy profiles. c) Representative conformations showing the interactions between NG^+/NG^n and the membrane in equilibrium simulations. d) Number of contacts between NG^+/NG^n and the bilayer as a function of simulation time. e) Order parameters of the NG^+-contact and NG^+-not contact lipids (labelled as bond n and bond n' in the middle panel) in the NG^+-bilayer complex simulations and order parameters of lipids in the NG^+ and NG^n simulations (right panel). The -Scd values of the three coarse-grained bonds are compared separately. Data are shown in the form of box plots, with the center line, box limits, and whiskers representing the median, upper and lower quartiles, and 1.5× interquartile range. f) 2-Dimensional density maps of lipid headgroups in NG^+ and NG^n simulations for the upper leaflet. The color scale represents the local number density, defined as the average count of headgroup beads per grid cell. Color gradients indicate local number density from depletion (red) to enrichment (blue). g) Mean curvatures of the membranes in NG^+ and NG^n simulations.

5. NG^+-engineered gap-junction-mimic interface enables directional inter-protocell macromolecule communication.

Directional contact and efficient material exchange between cellular communities represent a ubiquitous and crucial phenomenon in nature, serving as a fundamental driver for the emergence of primitive complex life through collision-induced activation. However, research in this domain remains limited to protocells,[78, 79] primarily focusing on small-molecule signal exchange with restricted investigation into the underlying mechanistic principles. Our previous exploration of NG^+-mediated protocell contact, assembly,

and transmembrane nanochannel formation suggests the potential to harness these properties for constructing gap-junction-mimic interfaces, which enable directional signal transduction and molecule-selective substance transport between protocells.

Therefore, building upon our previously demonstrated crucial interactions between NG^+ and protocell membranes, we engineered two distinct protocell populations ($FGUV^n$ and $BGUV^n$) loaded with fluorescent probe (10 kDa FITC-dextran) and quencher molecules (~600 Da BHQ1), respectively. In this system, the phospholipid membranes of BHQ1-containing $BGUV^n$ were labeled with DiI (displayed as blue in Figure 5a-d). Upon introducing NG^n and NG^+ to this binary protocell system, we observed remarkable differential effects (Figure 5a). While NG^n merely labeled both protocell membranes without enabling interpopulation communication, the NG^+-treated group exhibited a dramatic reduction of green fluorescence intensity in $FGUV^n$, indicating efficient FITC-dextran quenching by $BGUV^n$-encapsulated BHQ1 (Figure 5b). This characteristic quenching could also be observed through the ImageJ-based quantitative statistical and comparative analysis of intracellular FITC fluorescence intensity within the $FGUV^n$ protocells before and after the addition of NG^n and NG^+ (Figure S20). These results not only demonstrate NG^+-facilitated directional molecular exchange between protocell communities, but also reveal unidirectional transport characteristics, as evidenced by the absence of green fluorescence in $BGUV^n$.

Through systematic observation and analysis of NG^+-mediated interactions in the binary protocell communities, we conclude that this contact-induced inter-protocell communication establishes functional gap-junction-mimic interfaces (Figure 5c). These specialized interfaces simultaneously create robust mechanical linkages that firmly anchor adjacent protocells while forming precisely regulated nanochannels at membrane contact sites, thereby facilitating efficient molecular exchange between the coupled protocells. Furthermore, integration of these findings with our previous investigations and the experimental evidence presented in Figure 5b demonstrates that these biomimetic junctions exhibit size-selective permeability corresponding to the dimensions of the characterized nanochannels. This selective transport mechanism mediates passage of molecules with molecular weights below 10 kDa (representing relatively large molecules in this context), ultimately achieving directional inter-protocell communication. Moreover, to identify the factors influencing the directional characteristics of this inter-protocellular communication, we also designed a binary system comprising $FGUV^n$ protocells internally loaded with 4 kDa FITC-Dex and DiI-labeled GUV^n protocells internally loaded with the same concentration of 4 kDa dextran, while controlling the NG^+ treatment time to avoid excessive interaction intensity that could lead to dye leakage. Under these conditions, confocal microscopy images revealed negligible green fluorescence within the DiI-labeled protocells (Figure S21), indicating that in the absence of a concentration gradient difference, inter-protocellular signal communication does not occur even within the molecular weight directional limit. These results validate the directional characteristics of our gap-junction-mimic system as being simultaneously governed by molecular weight restriction and concentration gradient control.

Simultaneously, we validated this phenomenon by flow cytometry. Through quantitative analysis of the binary protocell population via the FITC fluorescence channel, we selectively identified the target $FGUV^n$ population (Figure 5d), thereby enabling monitoring of the quenching effect on FITC-dextran fluorescence. Flow cytometric analysis and MFI quantification of the targeted $FGUV^n$ subpopulation after interaction with NG^n or NG^+ revealed that while NG^n failed to mediate the transfer of quencher molecules from $BGUV^n$ to $FGUV^n$ for fluorescence quenching, NG^+ successfully facilitated this communication, resulting in significantly reduced FITC fluorescence intensity in the NG^+ group (Figure 5e,f). To exclude nanoparticle-specific artifacts, we designed control experiments by separately adding NG^n or NG^+ to $FGUV^n$ alone (Figure S22). The absence of significant FITC fluorescence changes in all control groups confirmed that neither NG^n nor NG^+ had intrinsic fluorescence-reducing effects. Therefore, the observed fluorescence reduction in $FGUV^n$ within the binary protocell population could only be attributed to NG^+-mediated communication with the quencher molecules in $BGUV^n$. Additionally, the SSC-A (Side Scatter-Area) and FSC-A (Forward Scatter-Area) data from flow cytometry characterization (Figure S23) indicated that the complexity of the protocells changed significantly before and after the addition of NG^n and NG^+, particularly in the NG^+- treated group. This further corroborates the aforementioned investigations regarding the strong interaction and significant impact of NG^+ on the membrane. In conclusion, via electrostatic interactions, NG^+ induces mutual contact between protocells in the binary population and generates gap-junction-mimic nanochannels at membrane contact sites, thereby enabling directional exchange of macromolecules and signals. This mechanism facilitates complex intercellular communication and promotes evolutionary development in artificial cellular systems.

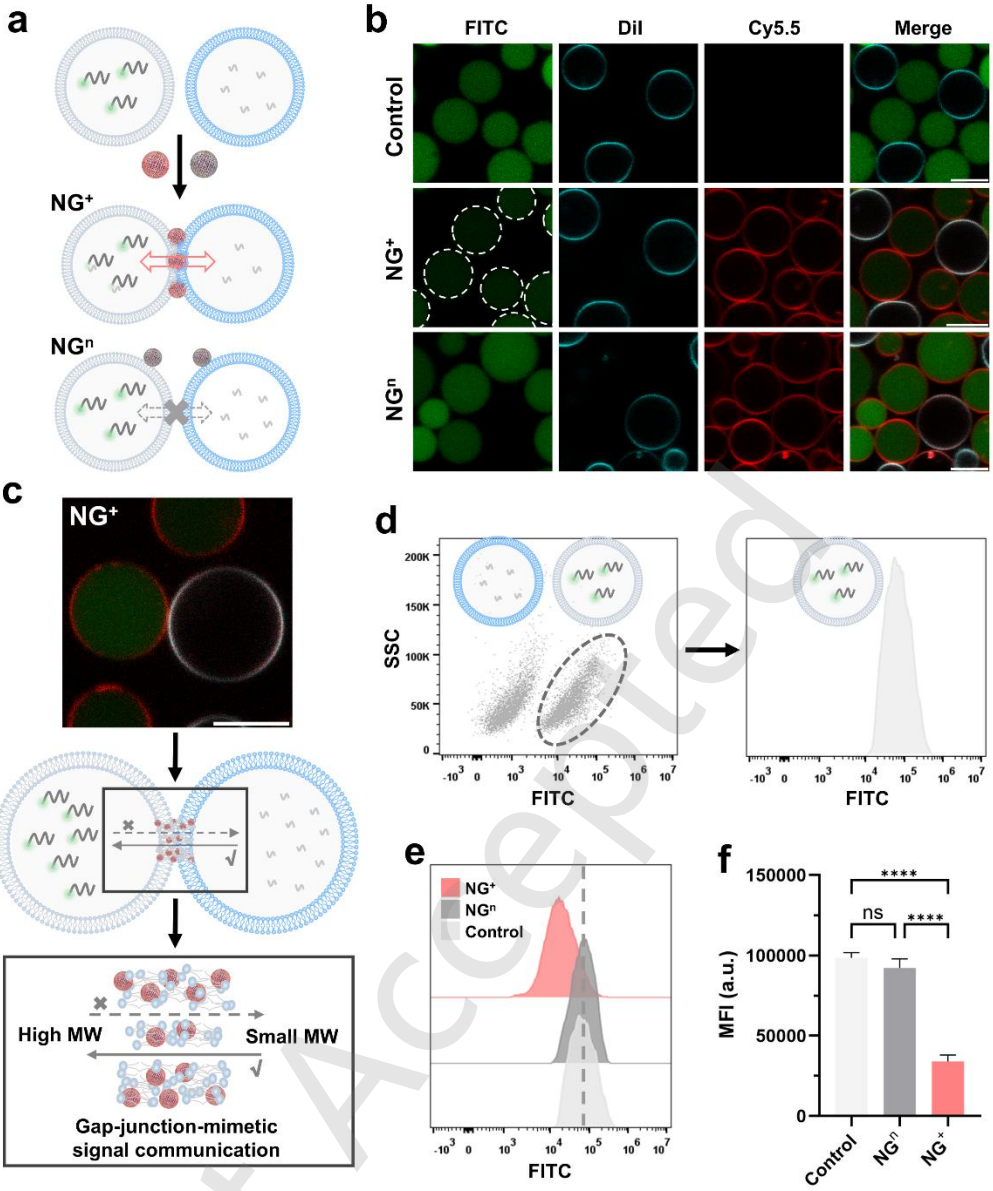

Figure 5. Designed binary protocell communities encapsulating distinct signaling molecules were interconnected through NG⁺-mediated gap-junction-mimic interfaces, enabling directional transmembrane signal communication between differentiated protocell populations. a) Schematic illustration highlighting NG⁺-mediated inter-protocell contact and subsequent transmembrane signaling communication between distinct protocell populations. b) Confocal microscopy images of binary protocell populations interact with NGs for 1 h, demonstrating NG⁺-mediated signal communication between two distinct protocell populations (FGUV^{n} and BGUV^{n}). Scale bars: 10 μm. c) Schematic illustration of NG⁺-induced gap-junction-mimic interfaces enabling molecule size-restricted directional signal communication between adjacent protocells. d) Flow-cytometric quantification of the binary protocell community, with FITC fluorescence employed to selectively identify the target FGUV^{n} population. e) Flow cytometry data and f) quantified analysis of MFI for the target FGUV^{n} subpopulation within binary protocell communities after 1 h co-incubation with NGs. Data were presented as the mean ± standard deviation (SD, n = 3).

Conclusions

In summary, we have systematically investigated the pivotal role and mechanistic underpinnings of electrostatic interactions in mediating nanoparticle-induced higher-order protocell assembly and inter-protocell communication. By exploiting gap-junction-mimic interfaces generated by NG⁺ on phospholipid membranes, we established a novel paradigm for signaling in binary protocell populations. The inherent negative charge of protocell membranes enables engineered NG⁺ to achieve spatiotemporal control, inducing protocell contact, interconnection, and higher-order assembly, which are the foundation for sophisticated population-level communication. Furthermore, leveraging the strong NG⁺-membrane interactions, we constructed transmembrane nanochannels and inter-protocell junctional interfaces, thereby pioneering signaling pathways between synthetic protocell communities. Complementary molecular dynamics simulations have not only validated our theoretical framework, but have also provided critical parametric insights into this communication strategy, particularly regarding charge density and disparity effects on membrane interactions and nanochannel dimensions. Although this simplified system cannot fully replicate

biological membrane complexity, it provides fundamental insights into the feasibility and mechanistic principles of electrostatically mediated interactions between cationic species and anionic membranes, with transformative implications for artificial cellular communication. Collectively, our systematic investigation of electrostatic interactions on phospholipid membranes extended to binary protocell communities has provided original insights into complex intercellular communication, while advancing approaches for exploring primitive life communication through bottom-up synthetic cellular engineering and pioneering potential perspectives for understanding dynamic communication processes among artificial cells.

Data availability

All data needed to support the conclusions in the paper are presented in the manuscript and the Electronic Supplementary Material. Additional data related to this paper may be requested from the corresponding author upon request.

Acknowledgements

We wish to gratefully acknowledge financial support from the Shanghai Science and Technology Plan Project (Grant no. 25J22800600), the STAR Program of Shanghai Jiao Tong University, Shanghai Collaborative Innovation Special Fund (Grant no. HCXBCY-2024-031) and the National Key R&D Program of China (Grant no. 2022YFE0100600) to H.D., as well as the Shanghai 2025 "Pioneer Initiative" Program (Grant no. 25XF3200100) and the Science and Technology Commission of Shanghai Municipality (Grant no. 25ZR1401202) to S.Y. We would also like to thank the Shanghai Jiao Tong University 2030 Initiative, the Fundamental and Interdisciplinary Disciplines Breakthrough Plan of the Ministry of Education of China for financial support, and the Instrumental Analysis Centre (IAC) of Shanghai Jiao Tong University for help with data characterization.

Declaration of competing interest

All the contributing authors report no conflict of interests in this work.

Author contribution statement

Q. X. G.: Theoretical work, experimental design, synthesis and characterization, methodology and writing. J. W. Z.: Molecular dynamics simulation related experiment. Y. H. Q.: Investigation, validation and formal analysis. Y. X. C.: Synthesis and characterization. S. Y.: Supervision and validation. R. X. G.: Molecular dynamics simulation, supervision and validation. H. J. D.: Conceptualization, supervision and project administration. This manuscript was written through the contributions of all authors. All authors have given approval to the final version of the manuscript.

Informed consent

Not applicable.

Ethics statement

Not applicable.

Use of AI statement

None.

References

[1] Maeda, S.; Nakagawa, S.; Suga, M.; Yamashita, E.; Oshima, A.; Fujiyoshi, Y.; Tsukihara, T. Structure of the connexin 26 gap junction channel at 3.5 Å resolution. Nature 2009, 458, 597-602.

[2] Wang, X.; Veruki, M. L.; Bukoreshtliev, N. V.; Hartveit, E.; Gerdes, H.-H. Animal cells connected by nanotubes can be electrically coupled through interposed gap-junction channels. Proc. Natl. Acad. Sci. U. S. A. 2010, 107, 17194-17199.

[3] Cen, Y.-Y.; Gao, X.-L.; Feng, Y.-H.; Zhou, C.; Li, C.-J.; Liu, F.; Shen, J.-F.; Zhang, Y.-Y. The Double-Edged Effect of Connexins and Pannexins of Glial Cells in Central and Peripheral Nervous System After Nerve Injury. Mol. Neurobiol. 2025, 10.1007/s12035-025-04991-6.

[4] Lee, J.-H.; Yang, S.-B.; Park, S. J.; Kweon, S.; Ma, G.; Seo, M.; Kim, H. R.; Kang, T.-B.; Lim, J.-H.; Park, J. Cell-Penetrating Peptide Like Anti-Programmed Cell Death-Ligand 1 Peptide Conjugate-Based Self-Assembled Nanoparticles for Immunogenic Photodynamic Therapy. ACS Nano 2025, 19, 2870-2889.

[5] Heili, J. M.; Stokes, K.; Gaut, N. J.; Deich, C.; Sharon, J.; Hoog, T.; Gomez-Garcia, J.; Cash, B.; Pawlak, M. R.; Engelhart, A. E.; Adamala, K. P. Controlled exchange of protein and nucleic acid signals from and between synthetic minimal cells. Cell Syst. 2024, 15, 49-62.e44.

[6] Wu, J.; Roesger, S.; Jones, N.; Hu, C.-M. J.; Li, S.-D. Cell-penetrating peptides for transmucosal delivery of proteins. J. Control. Release 2024, 366, 864-878.

[7] Zhang, L.; Liu, H.; Xu, H.; Wang, M.; Liu, H.; Li, W.; Zhang, C.; Han, W.; Chen, J.; Zhang, Y. In Situ Synthesis of Multifunctional 3D Polymeric Artificial Organelles in Living Cells. J. Am. Chem. Soc. 2025, 10.1021/jacs.5c08624.

[8] Zhu, T.; Chen, Z.; Jiang, G.; Huang, X. Sequential Targeting Hybrid Nanovesicles Composed of Chimeric Antigen Receptor T-Cell-Derived Exosomes and Liposomes for Enhanced Cancer Immunochemotherapy. ACS Nano 2023, 17, 16770-16786.

[9] Shi, Z.; Yan, J.; Zhao, M.; Li, S.; She, T.; Qian, X. Co-encapsulation of granzyme B and perforin in nanocapsules for tumour therapy: biomimicking immune cells. J. Control. Release 2024, 369, 658-667.

[10] Leung, C.; Hodel, A. W.; Brennan, A. J.; Lukoyanova, N.; Tran, S.; House, C. M.; Kondos, S. C.; Whisstock, J. C.; Dunstone, M. A.; Trapani, J. A.; Voskoboinik, I.; Saibil, H. R.; Hoogenboom, B. W. Real-time visualization of perforin nanopore assembly. Nat. Nanotechnol. 2017, 12, 467-473.

[11] Sun, L.; Hristova, K.; Bondar, A.-N.; Wimley, W. C. Structural Determinants of Peptide Nanopore Formation. ACS Nano 2024, 18, 15831-15844.

[12] Li, Q.; Shi, Z.; Ou, M.; Li, Z.; Luo, M.; Wu, M.; Dong, X.; Lu, L.; Lv, F.; Zhang, F.; Mei, L. pH-labile artificial natural killer cells for overcoming tumor drug resistance. J. Control. Release 2022, 352, 450-458.

[13] Gao, N.; Mann, S. Membranized Coacervate Microdroplets: from Versatile Protocell Models to Cytomimetic Materials. Acc. Chem.

Res. 2023, 56, 297-307.

[14] Belluati, A.; Thamboo, S.; Najer, A.; Maffeis, V.; von Planta, C.; Craciun, I.; Palivan, C. G.; Meier, W. Multicompartment Polymer Vesicles with Artificial Organelles for Signal-Triggered Cascade Reactions Including Cytoskeleton Formation. Adv. Funct. Mater. 2020, 30, 2002949.

[15] Bhat, A.; Huan, K.; Cooks, T.; Boukari, H.; Lu, Q. Probing Interactions between AuNPs/AgNPs and Giant Unilamellar Vesicles (GUVs) Using Hyperspectral Dark-field Microscopy. Int. J. Mol. Sci. 2018, 19, 1014.

[16] Inoue, Y.; Yoshinare, Y.; Yamaguchi, A.; Oshima, A.; Yamaguchi, M.; Heya, A.; Sumitomo, K. Aggregation Control of Gold Nanoparticles and Surface-Enhanced Raman Scattering within Giant Unilamellar Vesicles. Langmuir 2025, 41, 9567-9573.

[17] Abdollahi, N.; Messmer, D.; Mihali, V.; Palivan, C. G. Magnetically Controlled Polymer Giant Unilamellar Vesicles. Small 2025, n/a, 2502552.

[18] Moghimianavval, H.; Newell, C.; Parvizian, P.; Booth, M. J.; Liu, A. P. Strategies and applications of synthetic cell communication. Nat. Chem. Biol. 2025, 21, 1317-1329.

[19] Wang, M.; Nan, H.; Wang, M.; Yang, S.; Liu, L.; Wang, H.-H.; Nie, Z. Responsive DNA artificial cells for contact and behavior regulation of mammalian cells. Nat. Commun. 2025, 16, 2410.

[20] Su, J.; Song, Y.; Zhu, Z.; Huang, X.; Fan, J.; Qiao, J.; Mao, F. Cell–cell communication: new insights and clinical implications. Sig. Transduct. Target. Ther. 2024, 9, 196.

[21] Naz, M.; Mukwaya, V.; Yang, S.; Xiong, S.; Cruz, J. S.; Yu, X.; Tian, Z.; Dou, H. Matrix Assisted Assembly of Protocells into Multi-responsive Prototissues for Mechanical and Chemical Communication. Adv. Funct. Mater. 2024, 34, 2405781.

[22] Ikarashi, S.; Akai, H.; Koiwa, H.; Izawa, Y.; Takahashi, J.; Mabuchi, T.; Shoji, K. DNA Nanopore-Tethered Gold Needle Electrodes for Channel Current Recording. ACS Nano 2023, 17, 10598-10607.

[23] Yang, L.; Pecastaings, G.; Drummond, C.; Elezgaray, J. Driving DNA Nanopore Membrane Insertion through Dipolar Coupling. Nano Lett. 2024, 24, 13481-13486.

[24] Fan, S.; Wang, S.; Ding, L.; Speck, T.; Yan, H.; Nussberger, S.; Liu, N. Morphology remodelling and membrane channel formation in synthetic cells via reconfigurable DNA nanorafts. Nat. Mater. 2025, 24, 278-286.

[25] Yang, Q.; Guo, Z.; Liu, H.; Peng, R.; Xu, L.; Bi, C.; He, Y.; Liu, Q.; Tan, W. A Cascade Signaling Network between Artificial Cells Switching Activity of Synthetic Transmembrane Channels. J. Am. Chem. Soc. 2021, 143, 232-240.

[26] Li, L.; Liu, S.; Zhu, C.; Shao, S.; Yang, F.; Liu, Q.; Tan, W. DNA-Based Signal Circuit for Self-Regulated Bidirectional Communication in Protocell-Living Cell Communities. Angew. Chem. Int. Ed. 2025, 64, e202503903.

[27] Lv, C.; Gu, X.; Li, H.; Zhao, Y.; Yang, D.; Yu, W.; Han, D.; Li, J.; Tan, W. Molecular Transport through a Biomimetic DNA Channel on Live Cell Membranes. ACS Nano 2020, 14, 14616-14626.

[28] Llopis-Lorente, A.; Shao, J.; Ventura, J.; Buddingh', B. C.; Martínez-Máñez, R.; van Hest, J. C. M.; Abdelmohsen, L. K. E. A. Spatiotemporal Communication in Artificial Cell Consortia for Dynamic Control of DNA Nanostructures. ACS Cent. Sci. 2024, 10, 1619-1628.

[29] Chen, H.; Xu, W.; Shi, H.; Qiao, Y.; He, X.; Zheng, J.; Zhou, S.; Yang, X.; Wang, K.; Liu, J. DNA-Based Artificial Receptors as Transmembrane Signal Transduction Systems for Protocellular Communication. Angew. Chem. Int. Ed. 2023, 62, e202301559.

[30] Anton, J. S.; Iacovache, I.; Bada Juarez, J. F.; Abriata, L. A.; Perrin, L. W.; Cao, C.; Marcaida, M. J.; Zuber, B.; Dal Peraro, M. Aerolysin Nanopore Structures Revealed at High Resolution in a Lipid Environment. J. Am. Chem. Soc. 2025, 147, 4984-4992.

[31] Garcia-Fandiño, R.; Piñeiro, Á.; Trick, J. L.; Sansom, M. S. P. Lipid Bilayer Membrane Perturbation by Embedded Nanopores: A Simulation Study. ACS Nano 2016, 10, 3693-3701.

[32] Wu, F.; Jin, X.; Guan, Z.; Lin, J.; Cai, C.; Wang, L.; Li, Y.; Lin, S.; Xu, P.; Gao, L. Membrane Nanopores Induced by Nanotoroids via an Insertion and Pore-Forming Pathway. Nano Lett. 2021, 21, 8545-8553.

[33] Ying, Y.-L.; Hu, Z.-L.; Zhang, S.; Qing, Y.; Fragasso, A.; Maglia, G.; Meller, A.; Bayley, H.; Dekker, C.; Long, Y.-T. Nanopore-based technologies beyond DNA sequencing. Nat. Nanotechnol. 2022, 17, 1136-1146.

[34] Sun, K.; Zhao, C.; Zeng, X.; Chen, Y.; Jiang, X.; Ding, X.; Gou, L.; Xie, H.; Li, X.; Zhang, X.; Lin, S.; Dou, L.; Wei, L.; Niu, H.; Zhang, M.; Tian, R.; Sawyer, E.; Yuan, Q.; Huang, Y.; Chen, P.; Zhao, C.; Zhou, C.; Ying, B.; Shi, B.; Wei, X.; Jiang, R.; Zhang, L.; Lu, G.; Geng, J. Active DNA unwinding and transport by a membrane-adapted helicase nanopore. Nat. Commun. 2019, 10, 5083.

[35] Sihorwala, A. Z.; Lin, A. J.; Stachowiak, J. C.; Belardi, B. Light-Activated Assembly of Connexon Nanopores in Synthetic Cells. J. Am. Chem. Soc. 2023, 145, 3561-3568.

[36] Qiao, D.; Joshi, H.; Zhu, H.; Wang, F.; Xu, Y.; Gao, J.; Huang, F.; Aksimentiev, A.; Feng, J. Synthetic Macrocycle Nanopore for Potassium-Selective Transmembrane Transport. J. Am. Chem. Soc. 2021, 143, 15975-15983.

[37] Shen, J.; Gu, Y.; Ke, L.; Zhang, Q.; Cao, Y.; Lin, Y.; Wu, Z.; Wu, C.; Mu, Y.; Wu, Y.-L.; Ren, C.; Zeng, H. Cholesterol-stabilized membrane-active nanopores with anticancer activities. Nat. Commun. 2022, 13, 5985.

[38] Fu, Y.-H.; Hu, Y.-F.; Lin, T.; Zhuang, G.-W.; Wang, Y.-L.; Chen, W.-X.; Li, Z.-T.; Hou, J.-L. Constructing artificial gap junctions to mediate intercellular signal and mass transport. Nat. Chem. 2024, 16, 1418-1426.

[39] Chen, W.; Song, S.; Samanta, A.; Sethi, S.; Drees, C.; Kappl, M.; Butt, H.-J.; Walther, A. Growing functional artificial cytoskeletons in the viscoelastic confinement of DNA synthetic cells. Nat. Chem. Eng. 2025, 10.1038/s44286-025-00289-5, 627–639.

[40] Chakraborty, T.; Wegner, S. V. Cell to Cell Signaling through Light in Artificial Cell Communities: Glowing Predator Lures Prey. ACS Nano 2021, 15, 9434-9444.

[41] Mukwaya, V.; Mann, S.; Dou, H. Chemical communication at the synthetic cell/living cell interface. Communications Chemistry 2021, 4, 161.

[42] Xin, L.; Bai, D. Functional roles of the amino terminal domain in determining biophysical properties of Cx50 gap junction channels. Front. Physiol. 2013, 4, 373.

[43] Banach, K.; Ramanan, S. V.; Brink, P. R. The influence of surface charges on the conductance of the human connexin37 gap junction channel. Biophys. J. 2000, 78, 752-760.

[44] Srinivas, M.; Hopperstad, M. G.; Spray, D. C. Quinine blocks specific gap junction channel subtypes. Proc. Natl. Acad. Sci. U. S. A. 2001, 98, 10942-10947.

[45] Mondal, A.; Sachse, F. B.; Moreno, A. P. Modulation of Asymmetric

Flux in Heterotypic Gap Junctions by Pore Shape, Particle Size and Charge. Front. Physiol. 2017, 8, 206.

[46] Kanaporis, G.; Valiuniene, L.; Brink, P. R.; Valiunas, V. Gap Junction Permeability: Transfer of Negative and Positive Charged Probes. Biophys. J. 2009, 96, 287a.

[47] Guan, Q.; Chen, R.; Tian, Z.; Zhang, P.; Liu, L.; Cheng, M.; Zeng, Y.; Wu, D.; Zhou, M.; Dou, H. Electrostatic attraction-directed membrane anchoring as a universal tool to enhance nanocarrier uptake into drug-resistant cancer cells. Nano Res. 2025, 18, 94907906.

[48] Liu, L.; Zhang, Q.; Wang, C.; Guo, H.; Mukwaya, V.; Chen, R.; Xu, Y.; Wei, X.; Chen, X.; Zhang, S.; Zhou, M.; Dou, H. Single-Cell Diagnosis of Cancer Drug Resistance through the Differential Endocytosis of Nanoparticles between Drug-Resistant and Drug-Sensitive Cancer Cells. ACS Nano 2023, 17, 19372-19386.

[49] Qian, R.; Wu, M.; Yang, Z.; Wu, Y.; Guo, W.; Zhou, Z.; Wang, X.; Li, D.; Lu, Y. Rectifying artificial nanochannels with multiple interconvertible permeability states. Nat. Commun. 2024, 15, 2051.

[50] Fernandez, A.; Krishna, J.; Anson, F.; Dinsmore, A. D.; Thayumanavan, S. Consequences of Noncovalent Interfacial Contacts between Nanoparticles and Giant Vesicles. Angew. Chem. Int. Ed. 2022, 61, e202208616.

[51] Lin, J.; Zhang, H.; Chen, Z.; Zheng, Y. Penetration of Lipid Membranes by Gold Nanoparticles: Insights into Cellular Uptake, Cytotoxicity, and Their Relationship. ACS Nano 2010, 4, 5421-5429.

[52] Mukwaya, V.; Zhang, P.; Guo, H.; Dang-i, A. Y.; Hu, Q.; Li, M.; Mann, S.; Dou, H. Lectin-Glycan-Mediated Nanoparticle Docking as a Step toward Programmable Membrane Catalysis and Adhesion in Synthetic Protocells. ACS Nano 2020, 14, 7899-7910.

[53] Wang, B.; Zhang, L.; Bae, S. C.; Granick, S. Nanoparticle-induced surface reconstruction of phospholipid membranes. Proc. Natl. Acad. Sci. U. S. A. 2008, 105, 18171-18175.

[54] Yu, Y.; Granick, S. Pearling of Lipid Vesicles Induced by Nanoparticles. J. Am. Chem. Soc. 2009, 131, 14158-14159.

[55] Pogodin, S.; Werner, M.; Sommer, J.-U.; Baulin, V. A. Nanoparticle-Induced Permeability of Lipid Membranes. ACS Nano 2012, 6, 10555-10561.

[56] Wang, H.; Dai, T.; Li, S.; Zhou, S.; Yuan, X.; You, J.; Wang, C.; Mukwaya, V.; Zhou, G.; Liu, G.; Wei, X.; Dou, H. Scalable and cleavable polysaccharide nanocarriers for the delivery of chemotherapy drugs. Acta Biomater. 2018, 72, 206-216.

[57] Cheng, M.; Liu, L.; Zhang, P.; Xiong, S.; Dou, H. Cell Coding Arrays Based on Fluorescent Glycan Nanoparticles for Cell Line Identification and Cell Contamination Evaluation. ACS Appl. Mater. Inter. 2021, 13, 44054-44064.

[58] Zhang, P.; Mukwaya, V.; Guan, Q.; Xiong, S.; Tian, Z.; Levi-Kalisman, Y.; Raviv, U.; Xu, Y.; Han, J.; Dou, H. Dextran-based nanodrugs with mitochondrial targeting/glutathione depleting synergy for enhanced photodynamic therapy. Carbohydr. Polym. 2025, 348, 122854.

[59] Montes, L.-R.; Ahyayauch, H.; Ibarguren, M.; Sot, J.; Alonso, A.; Bagatolli, L. A.; Goni, F. M. Electroformation of Giant Unilamellar Vesicles from Native Membranes and Organic Lipid Mixtures for the Study of Lipid Domains under Physiological Ionic-Strength Conditions, 2010.

[60] Subramaniam, A. B.; Lecuyer, S.; Ramamurthi, K. S.; Losick, R.; Stone, H. A. Particle/Fluid Interface Replication as a Means of Producing Topographically Patterned Polydimethylsiloxane Surfaces for Deposition of Lipid Bilayers. Adv. Mater. 2010, 22, 2142-2147.

[61] Zhang, X.; Li, C.; Liu, F.; Mu, W.; Ren, Y.; Yang, B.; Han, X. High-throughput production of functional prototissues capable of producing NO for vasodilation. Nat. Commun. 2022, 13, 29571.

[62] Zong, W.; Ma, S.; Zhang, X.; Wang, X.; Li, Q.; Han, X. A Fissionable Artificial Eukaryote-like Cell Model. J. Am. Chem. Soc. 2017, 139, 9955-9960.

[63] Chibowski, E.; Szcześ, A. Zeta potential and surface charge of DPPC and DOPC liposomes in the presence of PLC enzyme. Adsorption 2016, 22, 755-765.

[64] Suetsugu, S.; Kurisu, S.; Takenawa, T. Dynamic Shaping of Cellular Membranes by Phospholipids and Membrane-deforming Proteins. Physiol. Rev. 2014, 94, 1219-1248.

[65] Kariuki, R.; Mirihana, K. A.; Penman, R.; Hung, A.; Meftahi, N.; Bryant, G.; Ramsland, P. A.; Voïtchovsky, K.; Conn, C. E.; Contini, C.; Bryant, S. J.; Christofferson, A. J.; Elbourne, A. Interactions of nanoparticles with living and synthetic bio-membrane. Chem. Soc. Rev. 2025, 10.1039/D5CS00841G, 10531-10615.

[66] Liu, M.; Huang, L.; Zhang, W.; Wang, X.; Geng, Y.; Zhang, Y.; Wang, L.; Zhang, W.; Zhang, Y.-J.; Xiao, S.; Bao, Y.; Xiong, M.; Wang, J. A transistor-like pH-sensitive nanodetergent for selective cancer therapy. Nat. Nanotechnol. 2022, 17, 541-551.

[67] Ewins, E.; Lira, R.; Zhang, W.; Yuan, J.; Antonietti, M.; Robinson, T.; Dimova, R. Poly(Ionic Liquid) Nanoparticles Selectively Disrupt Biomembranes. Adv. Sci. 2019, 6.

[68] Valeur, B.; Berberan-Santos, M. N. Molecular Fluorescence: Principles and Applications; Wiley: Weinheim, 2012.

[69] Bagatolli, L. A. To see or not to see: Lateral organization of biological membranes and fluorescence microscopy. Biochim. Biophys. Acta 2006, 1758, 1541-1556.

[70] Cai, C. X.; Zhu, H.; Chen, J. W. Overexpression of caveolin-1 increases plasma membrane fluidity and reduces P-glycoprotein function in Hs578T/Dox. Biochem. Bioph. Res. Co. 2004, 320, 868-874.

[71] Governa, M.; Valentino, M.; Visona, I.; Rocco, M. Impairment of Human Polymorphonuclear Leukocyte Chemotaxis by 2.5-Hexanedione. Cell Biol. Toxicol. 1986, 2, 33-39.

[72] Lv, Y.; Xu, C.; Zhao, X.; Lin, C.; Yang, X.; Xin, X.; Zhang, L.; Qn, C.; Han, X.; Yang, L.; He, W.; Yin, L. Nanoplatform Assembled from a CD44-Targeted Prodrug and Smart Liposomes for Dual Targeting of Tumor Microenvironment and Cancer Cells. ACS Nano 2018, 12, 1519-1536.

[73] Colom, A.; Derivery, E.; Soleimanpour, S.; Tomba, C.; Dal Molin, M.; Sakai, N.; Gonzalez-Gaitan, M.; Matile, S.; Roux, A. A fluorescent membrane tension probe. Nat. Chem. 2018, 10, 1118-1125.

[74] Arafiles, J. V. V.; Franke, J.; Franz, L.; Gomez-Gonzalez, J.; Kemnitz-Hassanin, K.; Hackenberger, C. P. R. Cell-Surface-Retained Peptide Additives for the Cytosolic Delivery of Functional Proteins. J. Am. Chem. Soc. 2023, 145, 24535-24548.

[75] Liu, X.; Yu, L.; Xiao, A.; Sun, W.; Wang, H.; Wang, X.; Zhou, Y.; Li, C.; Li, J.; Wang, Y.; Wang, G. Analytical methods in studying cell force sensing: principles, current technologies and perspectives. Regen. Biomater. 2025, 12, rbaf007.

[76] Yu, X.; Mukwaya, V.; Wang, L.; Zhao, W.; Mann, S.; Dou, H. Mechano-crosstalk between living and artificial cells. Nat. Commun. 2025, 16, 8582.

[77] Kästner, J. Umbrella sampling. WIREs: Comp. Mol. Sci. 2011, 1, 932-942.

[78] Sun, Y.; Lau, S. Y.; Lim, Z. W.; Chang, S. C.; Ghadessy, F.; Partridge, A.; Miserez, A. Phase-separating peptides for direct cytosolic delivery and redox-activated release of macromolecular therapeutics. Nat. Chem. 2022, 14, 274-283.

[79] Barba-Bon, A.; Salluce, G.; Lostalé-Seijo, I.; Assaf, K. I.; Hennig, A.; Montenegro, J.; Nau, W. M. Boron clusters as broadband membrane carriers. Nature 2022, 603, 637-642.

Electronic Supplementary Material

Inter-protocellular macromolecular communication via nanoparticle-induced gap-junction mimics

Qixiao Guan[1,§], Jianwen Zhang[2,§], Yonghui Qian[1], Yaxin Cui[1], Shuo Yang[1], Ruoxu Gu[2]✉, and Hongjing Dou[1]✉

[1] *The state Key Laboratory of Metal Matrix Composites, School of Materials Science and Engineering, Shanghai Jiao Tong University, Shanghai 200240, China*
[2] *School of Life Sciences and Biotechnology, Shanghai Jiao Tong University, Shanghai 200240, China*
[§] Qixiao Guan and Jianwen Zhang contributed equally to this work.

✉ Address correspondence to Ruoxu Gu, mircial@sjtu.edu.cn; Hongjing Dou, hjdou@sjtu.edu.cn

Supporting information to https://doi.org/10.26599/NR.2026.94908733

Table of Contents

1. Experimental Section

Materials

Dextran (Dex, Mw = 40,000 Da), chitosan oligosaccharide (COS) and glacial acetic acid were purchased from TCI. Ceric ammonium nitrate (CAN, >99%), methyl acrylate (MA) and N,N-methylene-bis-acrylamide (MBA) were purchased from Sigma-Aldrich. The pure methyl acrylate was obtained by removing polymerization inhibitor and other impurities through vacuum distillation. MBA was dissolved and washed with a mixed solution of ethanol and dimethylformamide, and then recrystallized to obtain purified MBA. Glycidyltrimethylammonium chloride (GTMAC), succinic anhydride (SA) and 4-dimethylaminopyridine (DMAP) were purchased from Sigma-Aldrich. Meanwhile, the Cy5.5 (Cyanine 5.5) NHS ester (non-sulfonated) was purchased from GlpBio. Fluorescence quencher BHQ1-NHS (BHQ1) was purchased from MCE.

1-Palmitoyl-2-oleoyl-sn-glycero-3-PC (POPC), cholesterol, glucose, sucrose, 3,3'-dioctadecyloxacarbocyanine perchlorate (DiO), 1,1'-dioctadecyl-3,3,3',3'-tetramethylindocarbocyanine perchlorate (DiI), and 1,6-diphenyl-1,3,5-hexatriene (DPH) were obtained from Sigma-Aldrich. 2,3-Dioleoyloxy-propyl-trimethylammonium-chloride (DOTAP) and 1,2-dioleoyl-sn-glycero-3-phosphoric acid (DOPA) were obtained from Avanti Polar. 1,1'-[1,4-Phenylenebis(methylene)]-bis(1-pyridinium) dibromide (DPX) and disodium 8-amino-1,3,6-naphthalenetrisulfonate (ANTS) were purchased from TCI. FITC-Dextran with different molecular weights (750 Da, 1 kDa, 4 kDa, and 10 kDa) were purchased from Aladdin. Meanwhile, the Flipper-TR membrane tension probe was purchased from Spirochrome. All other reagents and solvents were purchased from Adamas unless specified. Milli-Q purified water (18.2 MΩ cm) was used for all the experiments.

Preparation of the charged nanoparticles

To obtain charged nanoparticles, we modified and improved upon previous research,[1-3] utilizing the graft copolymerization-induced self-assembly (GISA) strategy to synthesize glycan nanogels with positive, negative, and neutral charges. For neutral glycan nanoparticles (NG^n), dextran (400 mg, approximately 2.5 mmol based on the molecular weight of the glycan unit) was dissolved in 20 mL of Milli-Q water, kept under N_2 protection, and gently stirred for 30 min at 30 °C. The initiator CAN (193 mg dissolved in 0.5 mL of 0.1 N nitric acid) was then added, and 5 min later, the monomer MA (225 μL) was added dropwise into the solution. The crosslinker MBA (38 mg dissolved in 2 mL of Milli-Q water) was added dropwise into the system 30 min after the addition of the MA. The molar ratio of glycan units to methyl acrylate was 1:1. The reaction proceeded at 30 °C for 4 h. The crude product was subsequently purified via dialysis against Milli-Q water for 3 days to yield the NG^n.

For positively charged nanoparticles (NG^+), we first synthesized quaternized chitosan oligosaccharides (qCOS). The qCOS was synthesized via one-pot reaction between epoxy groups from glycidyltrimethylammonium chloride (GTMAC) and the amino groups of chitosan oligosaccharide.[4, 5] Specifically, 2 g of chitosan oligosaccharide was suspended in 72 mL of Milli-Q water, and then 500 μL of glacial acetic acid was added to the suspension. After stirring at 60 °C for 30 min, 7.38 g of GTMAC solution were added dropwise to the mixture under continuous stirring. The molar ratio of GTMAC to amino groups on the glycan backbone was 5:1. The reaction mixtures were stirred at 60 °C for 12 h. The crude product was dialyzed exhaustively (using dialysis bags with a molecular weight cut off (MWCO) of 3500 or 1000 Da) against Milli-Q water for 3 days in the dark condition, and the pure product was obtained by lyophilization. In order to prepare positively charged nanoparticles, the overall process of preparation was roughly the same as described above. The adjustment included the glycan portion composed of both Dex and qCOS, and the glycan units ($N_{Dex\text{-}Glu}/N_{qCOS\text{-}Glu}$) molar ratio was 1:3, while the overall process and relevant mole ratio remained unchanged.

For negatively charged nanoparticles (NG^-), we first synthesized a nanogel (CNG) with Dex and COS as the glycan components to provide amino groups that can be further modified. The synthesis process was similar to the one mentioned earlier, with the only difference being that the glycan components were Dex and COS, and the glycan units ($N_{Dex\text{-}Glu}/N_{COS\text{-}Glu}$) molar ratio was 1:3. Subsequently, the purified CNG obtained by dialysis was freeze-dried. Following this step, 120 mg of

freeze-dried CNG and 180 mg of succinic anhydride were suspended in 15 mL of dimethyl sulfoxide (DMSO) at 60 °C for 30 min, followed by the addition of 5 mg of DMAP as a catalyst. The reaction mixture was left to stir for 16 h. After the reaction, the mixture was diluted with 30 mL Milli-Q water and dialyzed extensively (MWCO = 3500 Da) against Milli-Q water for 3 days.

To obtain Cy5.5-labeled NGs, 2 mL of NGs (10 mg/mL dispersed in water) and 0.9 mL of DMSO were mixed, causing swelling of the nanogels. Subsequently, 0.1 mL of Cy5.5-NHS (2.5 mg/mL pre-dissolved in DMSO) was added to the mixture. Then, 5 mL of Milli-Q water was slowly added to the mixture under an oscillation condition of 1000 rpm. The mixture was oscillated for 2 h and went through dialysis with Milli-Q water until no fluorescence signal could be detected in the external dialysate solution.

To obtain quencher molecule BHQ1-labeled NGs (QNGs), 2 mL of NGs (10 mg/mL dispersed in water) and 0.9 mL of DMSO were mixed, causing swelling of the nanogels. Subsequently, 0.1 mL of BHQ1-NHS (2.5 mg/mL pre-dissolved in DMSO) was added to the mixture. Then, 5 mL of Milli-Q water was slowly added to the mixture under an oscillation condition of 1000 rpm. The mixture was oscillated for 2 h and went through dialysis with Milli-Q water.

Preparation of the protocell model vesicles

To mimic the native phospholipid constitution of biological membranes, we designed and synthesized natural giant unilamellar vesicles (GUV^n) as protocell model vesicles using the electroformation method, which was applied by following the modified protocol.[6-8] Specifically, POPC, cholesterol, and DiO were dissolved separately in anhydrous chloroform to prepare stock solutions of 10 mM, 20 mM, and 0.1 mM, respectively. Subsequently, 6.4 μL of POPC (10 mM), 1.2 μL of cholesterol (20 mM), and 1 μL of DiO (0.1 mM) were combined to achieve a molar ratio of 70:30:1 (POPC:cholesterol:DiO) and this mixture was homogenized via thorough Vortex treatment. The mixed lipid solution was then transferred onto Indium Tin Oxide (ITO)-coated glass slides and dried at atmospheric pressure for at least 1 h. The dried thin film was then slowly filled with 350 μL of 300 mM sucrose aqueous solution. The production of GUV^n in the electroformation chamber (Nanion Vesicle Prep Pro) was performed as follows. GUV^n were produced under voltage of 2 V and frequency of 10 Hz at 37 °C for 2 h, followed by pipetting gently and washing with an equal volume of 300 mM aqueous glucose solution. Then the solution was centrifuged (37 °C, 300 g) for 3 min, and the pellet was washed at least three times with 1 mL of 300 mM glucose solution to remove the free substances. The pellet was resuspended in 1 mL of 300 mM aqueous glucose solution and stored at 4 °C for further use. The concentration of the GUVs stock solution was determined at around 2×10^5 number/mL.

For the synthesis of GUV^+ and GUV^-, the phospholipid POPC used in the preparation of GUV^n was replaced with DOTAP (2,3-Dioleoyloxy-propyl-trimethylammonium-chloride) and DOPA (1,2-dioleoyl-sn-glycero-3-phosphoric acid), respectively, while keeping all other experimental procedures unchanged.

Similarly, both $FGUV^n$ encapsulating FITC-Dextran internally and $WFGUV^n$ containing FITC-Dextran of varying molecular weights in the external environment were synthesized using analogous methods. The key difference was the removal of the DiO membrane fluorescent dye during the initial electroformation step. For $FGUV^n$, 4 kDa FITC-Dextran was initially dissolved in 300 mM sucrose aqueous solution at a concentration of 62.5 μg/mL. The solution was then introduced into the electroformation chamber to generate $FGUV^n$. Subsequently, the vesicles were washed and resuspended in glucose solution (300 mM) to obtain purified $FGUV^n$ with encapsulated FITC-Dextran.

For the preparation of DiI-labeled $BGUV^n$, the synthesis protocol involved substituting FITC-Dextran in the $FGUV^n$ procedure with BHQ1, while additionally incorporating DiI as the membrane fluorescent dye in place of DiO used in previous procedures, with all other experimental procedures unchanged.

For $WFGUV^n$, FITC-Dex of different molecular weights was first dissolved in 300 mM glucose solution at a concentration of 62.5 μg/mL. After an electroformation reaction had been conducted in the chamber, the resulting GUV^n were washed three times with glucose solution containing the corresponding molecular weight of FITC-Dextran. Subsequently, the pellet was resuspended in the same solution to obtain $WFGUV^n$ with externally localized FITC-Dextran of varying molecular weights.

Characterization of the nanoparticles and vesicles

The morphologies of NG^+, NG^n, and NG^- were characterized via transmission electron microscopy (TEM) utilizing a Tecnai G2 Spirit BioTwin Transmission Electron Microscope (FEI-Thermo Fisher Scientific, USA). The morphologies of the protocell model vesicles (GUV^n, GUV^-, GUV^+, $FGUV^n$, and $WFGUV^n$) were characterized via confocal laser scanning microscopy (CLSM). In addition, the particle sizes of the samples were statistically analyzed using ImageJ software. Zeta potential measurements of the samples were performed with a Zetasizer Nano ZS90 Instrument (Malvern, UK). Additionally, the hydrodynamic diameter and colloidal dispersibility of the various nanoparticles in Milli-Q water were measured via dynamic light scattering (DLS) characterization at a sample concentration of 0.8 mg/mL with a Zetasizer Nano ZS90 Instrument (Malvern, UK). Fluorescence spectra were recorded with an RF-6000 Spectrofluorophotometer (Shimadzu, Japan).

Analysis of nanoparticle–protocell interactions

The interactions between NGs and protocell model vesicles were characterized by flow cytometry and confocal laser scanning microscopy (CLSM), followed by comprehensive data analysis.

For flow cytometry, the protocells were seeded in a 1.5 mL Eppendorf tube at a density of 2×10^5 number/tube, and incubated with NGs at a concentration of approximately 60 μg/mL at specific temperatures (default room temperature unless otherwise specified) for a specified time (default co-incubation time is 2 h unless otherwise specified). After incubation, the protocells were finally analyzed with a Cytoflex Flow Cytometer (Beckman Colter, USA). Channels: FITC, APC-A700 (for Cy5.5). The results were analyzed using FlowJo V10 software, and the mean fluorescence intensity (MFI) was recorded for quantitative assessment.

For CLSM, the protocells were seeded in a glass-bottomed dish at a density of 5×10^4 number/dish, and incubated with NGs at a concentration of approximately 60 μg/mL at room temperature for a specified time (default co-incubation time is 2 h unless otherwise specified). After incubation, the protocells were finally visualized under a Leica STELLARIS 5 Confocal Microscope (Leica, Germany). FITC and DiO were both excited with the 488 nm line of an argon laser, DiI was excited with a 561 nm laser, and Cy5.5 was excited with a 633 nm laser. Image intensity quantification was performed in the Leica software (Leica Application Suite) using an intensity line profile. Then, from confocal microscopy images acquired across three independent replicate experiments, the average fluorescence intensity of 50 randomly selected vesicles within the field of view was quantified using ImageJ software.

Microscale investigation of NG^+-protocell interactions

Microscale nano-protocells were prepared using the thin film hydration method, which is a classic liposome preparation method.[9, 10] Briefly, POPC and cholesterol were mixed in chloroform at a molar ratio of 7:3, maintaining the same ratio as macroscale protocells. A lipid chloroform solution (2 mL) containing 3.5 mM POPC and 1.5 mM cholesterol was added to a 10 mL round-bottom flask, and the sample was quickly spread over the entire surface of the flask. After evaporating the lipid solution into a thin film using rotary evaporator, it was vacuum dried at 37 °C for 4 h to remove residual traces of solvent. The lipid thin film was then resuspended in a sucrose aqueous solution and vortexed at 37 °C to form a milky and uniform suspension. The resuspended lipid solution was sonicated in a 10 mL round-bottom flask for 1 min using an ultrasonic probe at a frequency of 24 kHz and power of 60 W. Subsequently, the resulting vesicles were extruded 21 times serially through 1000 nm, 800 nm, and 400 nm polycarbonate porous membranes using an Avanti mini extruder (Avanti Polar Lipids) to obtain the nano-protocells. Lastly, the final target nano-protocells were obtained by thorough dialysis (MWCO = 3500 Da) against glucose solution for 24 h in the dark.

After interacting with NG^+ for 1 h, the key characteristics of NG^+ induced mutual interactions with nano-protocells were characterized via TEM utilizing a Tecnai G2 Spirit BioTwin Transmission Electron Microscope (FEI-Thermo Fisher Scientific, USA). In addition, the enhanced resolution and structural detail were characterized via Cryo-TEM utilizing a Talos F200C G2 field emission transmission electron microscope (FEI-Thermo Fisher Scientific, USA).

Dye-encapsulated nano-protocells were prepared using the similar methodology and formulation as previously described. In contrast to the previous procedure, the dried thin film was subsequently hydrated with 2 mL of dye solution (10 mM Na_2HPO_4) containing DPX (19.0 mg/mL) and ANTS (5.35 mg/mL). Subsequently, the dye-encapsulated nano-protocells were incubated with NG^n and NG^+. After 30 min of incubation, dye leakage was monitored by a spectrofluorophotometer. Nano-protocells that had not received additional treatments were used as the negative control, and those treated with 0.1% TritonX-100 were used as the positive control. The percentage of dye release from the nano-protocells was calculated as $[(I_{\text{sample}} - I_{\text{negative control}}) / (I_{\text{positive control}} - I_{\text{negative control}})] \times 100\%$.

NGs induced membrane fluidity change

We primarily utilized two methods to measure and cross-validate protocell membrane fluidity. First, we used the FRAP (Fluorescence Recovery After Photobleaching) mode of the confocal microscope to detect membrane fluidity. Second, we characterized membrane fluidity by measuring fluorescence anisotropy using the DPH probe.

1) For the FRAP method, after co-incubation of NGs and protocells, fluorescence recovery after photobleaching experiments were conducted using a Leica STELLARIS 5 confocal microscope with a 100× objective lens. For protocells, specific regions of interest (ROIs) were bleached with a 488 nm laser for DiO or a 633 nm laser for Cy5.5, respectively, over 8 iterations of 0.863 s at 100% power. The fluorescence recovery of the bleached areas was recorded over a duration of 45 s. The fluorescence intensity of the bleached area was background-subtracted, normalized to the fluorescence intensity of the first postbleach image.

2) For the DPH probe method,[11-13] the protocells were first labeled with DPH probe at a final concentration of 2 μM dispersed in a glucose aqueous solution. After incubation for 30 min at 37 °C, the protocell suspensions were centrifuged and washed twice with glucose solution at 300 g for 3 min. The protocells were finally resuspended in glucose solution, and co-incubated with NGs for 2 h. Subsequently, the fluorescence anisotropy was immediately measured in a FLS1000 Spectrofluorometer (Edinburgh Instruments, UK). The excitation and emission wavelengths were 360 and 430 nm, respectively. The fluorescence polarization value (P) was calculated by equation (1):

$$P = \frac{I_{V-V} - G \times I_{V-H}}{I_{V-V} + G \times I_{V-H}} \quad (1)$$

The grating factor, G, is given by the instrument.

NGs induced membrane tension change

The protocells were first suspended in glucose solution at a density of 2×10^5 number/tube, then centrifuged to obtain the bottom pellet, followed by the addition of 300 μL of Flipper-TR membrane tension probe working solution prepared according to the manufacturer's instructions, and co-incubated at 37 °C for 20 minutes. Afterward, the protocell suspensions were centrifuged and washed twice with glucose solution at 300 g for 3 min. The protocells were then ready for observation using fluorescence lifetime imaging microscopy (FLIM) with the MicroTime 200 Single-molecule Time-resolved Confocal Microscope (PicoQuant, Germany). In the next step, NGs were directly added, and after the appropriate incubation time, further FLIM observations were conducted. Finally, a double exponential fit was applied to the fluorescence decay (τ).

NGs induced macroscopic stiffness variations in protocells

Atomic Force Microscopy (AFM) force measurements were conducted using a Bio-FastScan scanning probe microscope (Bruker). AFM force measurements were conducted in liquid under ambient conditions. The protocell suspensions (including untreated control and NGs-treated samples after 30 min co-incubation) were added dropwise and fixed onto a polylysine-coated glass coverslip. Commercially available AFM ball tips with a radius of 6 μm were used (spring constant of 0.01 N/m, deflection sensitivity of 37 nm/V). The results obtained from AFM were processed by NanoScope Analysis (Bruker) software,

and the Young's modulus was calculated by fitting the data with the Hertzian model.

Coarse-Grained model of polysaccharide nanogels

We constructed the coarse-grained models of NG^+ and NG^n under the framework of Martini 3.[14] We first parameterized the monomers (e.g., monosaccharides) and then constructed the topology of the polymers using Polyply.[15]

Specifically, the all-atom structures of monosaccharide units of COS (MonoCOS) and monosaccharide units of qCOS (MonoqCOS) were mapped to coarse-grained beads (see Figure S18b), and the bonded interactions were parameterized based on their conformations in atomistic simulation trajectories using the CHARMM36m force field. To enhance the hydrophilicity of the saccharides and reduce their self-association, the Lennard-Jones interactions between TC4 beads of the saccharides and water beads were increased three-fold. The parameters of glucose and the monomers of polymethyl acrylate (PMA) were adopted from literatures,[15, 16] with the Lennard-Jones interactions between the beads constituting PMA increased two-fold to maintain the formation of a nanoparticle in simulations.

The polymers constituting the nanogels can be divided into two parts: a polysaccharide and a PMA (Figure S18a). The electrically natural polysaccharide chains in the NG^n nanoparticle were modeled as polymers with 60 glucose units through α-1,6 glycosidic bonds, with 6 open-ring residues each grafted with a PMA chain composed of 10 methyl acrylate monomers. The positively charged polysaccharide chains in the NG^+ nanoparticle were built based on 20 monosaccharides, with alternating arrangement of monoCOS and monoqCOS, among which two open-ring monoCOS residues were each linked to a PMA chain with 10 monomers. These monosaccharides (monoCOS and monoqCOS) were polymerized through β-1,4 glycosidic bonds, whose parameters were taken from the cellulose force field[15] due to their identical linkage type. NG^n nanoparticles in our simulations were constituted by four polymers with electrically natural glucan chains, while the NG^+ nanoparticles were composed of two electrically natural polymers (glucan chains) and six positively charged polymers. A number of polymers were first solvated by water molecules, and equilibrium molecular dynamics simulations were then performed, during which these polymers aggregated to form nanoparticles in a spontaneous manner.

Our coarse-grained model was validated by comparing the coarse-grained and atomistic results of the following simulations: i) we calculated the oil-water partition free energy profiles of glucose, monoCOS and monoqCOS in biphasic water-hexadecane systems using the umbrella sampling method[17] (Figure S18d); ii) we conducted simulations of hepta-saccharide chains for cellulose, COS and qCOS and calculated their radius of gyration (R_g) and end-to-end distances (Figure S18c,e). In these simulations, we employed CAHRMM36m force field[18-23] for the atomistic simulations and constructed the all-atom polysaccharide models by CHARMM-GUI.[24] In addition, we also performed equilibrium simulations started from an initial conformation with a number of randomly distributed polymers and confirmed whether or not they can assemble a compact nanoparticle spontaneously (NG^n or NG^+), as mentioned above.

Molecular dynamics simulations of nanoparticle-membrane interactions

We conducted both non-equilibrium and equilibrium simulations to investigate the interactions between polysaccharide nanogels and membranes. Specifically, in the non-equilibrium simulations, we used the umbrella sampling method to calculate the free energy profile of one nanoparticle (NG^n or NG^+) approaching the bilayer as a function of the distance between their centers of mass. While in the equilibrium simulations, 5 nanoparticles (either NG^n or NG^+) were positioned randomly around the membrane, and 10 μs simulations were then performed to explore their interactions. In both simulations, we employed a binary mixture of POPC and cholesterol with a molar ratio of 7:3 and a bilayer dimension of 30 nm × 30 nm.

Parameters of Molecular Dynamics Simulations

All simulations were conducted using GROMACS2023.5. The coarse-grained simulations employed the Martini 3 force field[14] and an integration time step of 20 fs. A velocity-rescale thermostat[25] was used to maintain the system at 300 K with a relaxion time step of 1 ps and separate coupling of the bilayer, solvent and nanoparticles, while the pressure was

constrained at 1 bar using the Parinello-Rahman barostat[26, 27] and a semi-isotropic coupling method with a relaxion time step of 12 ps and a compressibility of 3.4 $\times 10^{-4}\ bar^{-1}$. A cutoff value of 1.1 nm and the potential shift Verlet algorithm were applied to calculate the van der Waals interactions, while the same cutoff value and the reaction field method[28] were used to tackle the electrostatic interactions. All bonds were constrained using the LINCS algorithm.[29] For all-atom simulations, we used the CHARMM36m force field[18-23] with an integration time step of 2 fs. The temperature was constrained at 300 K using the velocity rescale thermostat,[25] with a relaxation time step of 1 ps and separate coupling of the solvent and solute groups, while the C-rescale barostat[30] was employed to maintain the pressure semi-isotropically at 1 bar with a compressibility of 4.5 $\times 10^{-5}\ bar^{-1}$ and a relaxation time step of 5 ps. Van der Waals interactions were treated with a force switching cutoff scheme, which were turned off gradually from 1.0 to 1.2 nm, while the long range electrostatic interactions were computed using the particle mesh Ewald (PME) method[31, 32] with a real space cutoff value of 1.2 nm, a Fourier grid spacing of 0.12 nm and an interpolation order of 4. All hydrogen-containing bonds were constrained using the LINCS algorithm.[29]

We used the umbrella sampling method[17] to calculate the free energy profile of one nanoparticle approaching the membrane. Specifically, we employed the distance along the *z*-axis between the centers of mass of the nanoparticle and the bilayer as the reaction coordinate. In particular, 34 sampling windows were used, which were spaced at intervals of 0.1 nm. The initial conformation of each window was generated by pulling the particle along the reaction coordinate, and each window was sampled for 50 ns with the reaction coordinate restrained at desired values using a force constant of 1000 kJ mol^{-1} nm^{-2}. The free energy profiles were reconstructed using the weighted histogram analysis method (WHAM) as implemented in GROMACS.[33]

In addition, we also used the umbrella sampling method to calculate the oil-water partition free energy profile in a biphasic water-hexadecane system for three monosaccharides (glucose, monoCOS, and monoqCOS) at both the coarse-grained and all-atom levels. At both levels, we used the distance between the center of mass of the solute molecule and the center of mass of the aqueous phase along the interface normal as the reaction coordinate, with 38 (glucose and monoCOS) or 48 (monoqCOS) sampling windows spaced every 0.1 nm. The initial conformation of each window was generated by Packmol.[34] Each window was sampled for 10 ns with a force constant of 1000 kJ mol^{-1} nm^{-2} at the all-atom level and 7 ns with a force constant of 1000 kJ mol^{-1} nm^{-2} at the coarse-grained level. The free energy profiles were also reconstructed using the weighted histogram analysis method[33] with a boot strap error estimation.

Data Analysis

Lipid tail order parameter (-Scd) was calculated according to the following equation (2):

$$-Scd = -(3\cos^2\theta - 1)/2 \quad (2)$$

where θ was the angle between the vector connecting two coarse-grained beads from the lipid tail and the z-axis. For the NG$^+$-bilayer system, the POPC lipids were categorized into two groups based on whether they contact with the nanoparticle: they are considered to have contacts if the distance between any of the lipid beads and NG$^+$'s beads is smaller than 0.5 nm. We then compared the order parameters of the lipids that contact and non-contact with the nanoparticles. We also compared order parameters of all of the lipids in the NG$^+$ containing and NG^n containing systems. To further quantify the nanoparticle-membrane interaction strength, the number of contacts was determined by counting the number of nanoparticle beads located within 0.5 nm of any lipid headgroup bead.

The 2-dimensional density of lipid headgroups was calculated for the two leaflets separately. Specifically, the bilayer plane was discretized into a 2-dimensional grid with a grid width of 0.5 nm, and the number of headgroup beads in each grid was counted and averaged over simulation time.

We also calculated the curvature of the two membrane leaflets in equilibrium simulations. The bilayer plane was discretized into a 2-dimensional grid with a grid width of 1.2 nm, and a reference surface was constructed based on the PO4 beads of the lipids, from which the mean and Gaussian curvature were computed and averaged over simulation time. All of the

above analyses were facilitated by the MDAnalysis module,[35, 36] and the last 1 μs trajectory was used in these analyses.

Statistical analysis and reproducibility

Statistical parameters, including the definitions and exact values of *n* (for example, number of experiments, number of protocells, and so on), distributions and deviations are reported in the figures and corresponding figure legends. All experiments were repeated at least three times, and all data are expressed as mean ± standard deviation (SD) unless otherwise specified. For comparison between two data sets, the statistical analysis was determined using a two-tailed Student's *t*-test. For more data sets, the statistical analysis was determined using a one-way analysis of variance. In addition, the statistical significance was set at *p*-values of (*) $p < 0.05$, (**) $p < 0.01$, (***) $p < 0.001$, and (****) $p < 0.0001$. Values were normally distributed and the variance was similar between the compared groups. $P < 0.05$ was considered statistically significant.

2. Supplementary Figures

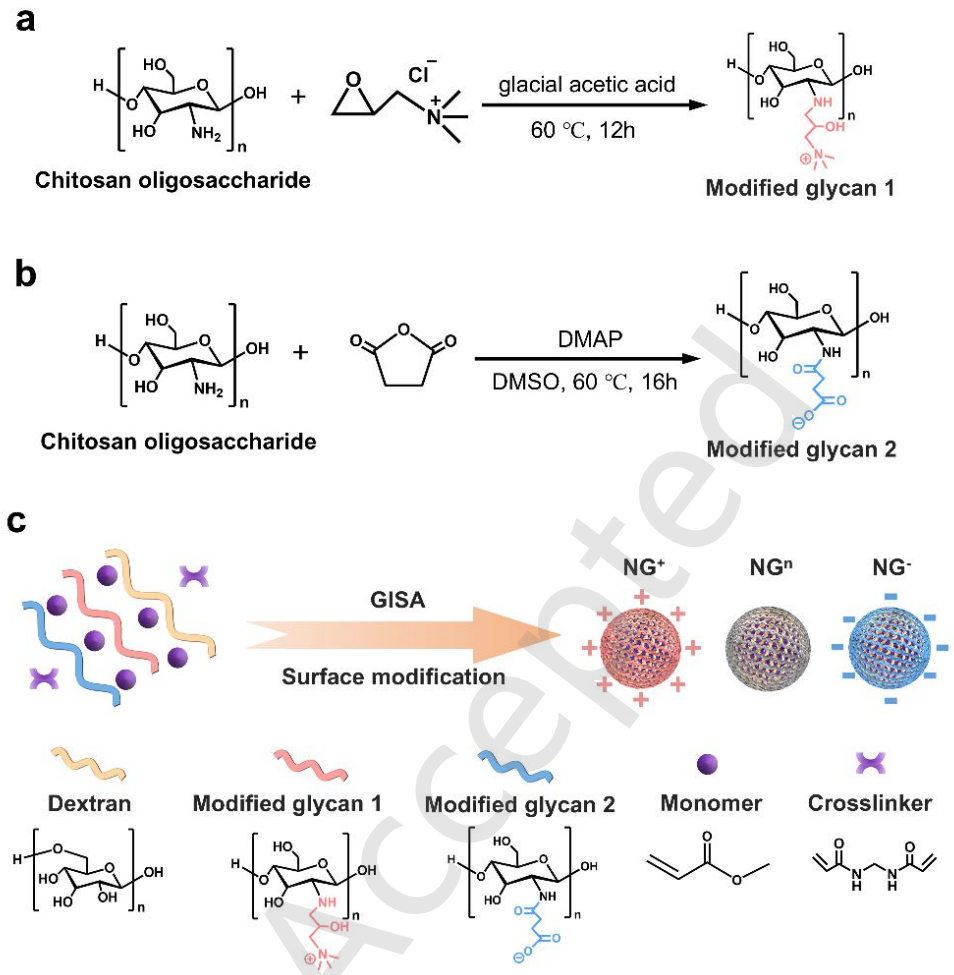

Figure S1. Schematic illustration showing the synthetic routes and surface modification process for charged nanoparticles. (a) Synthetic pathway for the grafting of cationic functionalities onto polysaccharide scaffolds. (b) Synthetic pathway for the grafting of anionic functionalities onto polysaccharide scaffolds. (c) Schematic diagram of the preparation process for positively charged nanoparticles (NG^+), neutral nanoparticles (NG^n), and negatively charged nanoparticles (NG^-). Briefly, we implemented a graft copolymerization-induced self-assembly (GISA) strategy by conducting graft copolymerization of hydrophobic chains on polysaccharide backbones to construct polysaccharide nanogel particles (NGs) via subsequent self-assembly, while utilizing the facile modifiability of polysaccharide structures to introduce charged groups for imparting different charge characteristics.

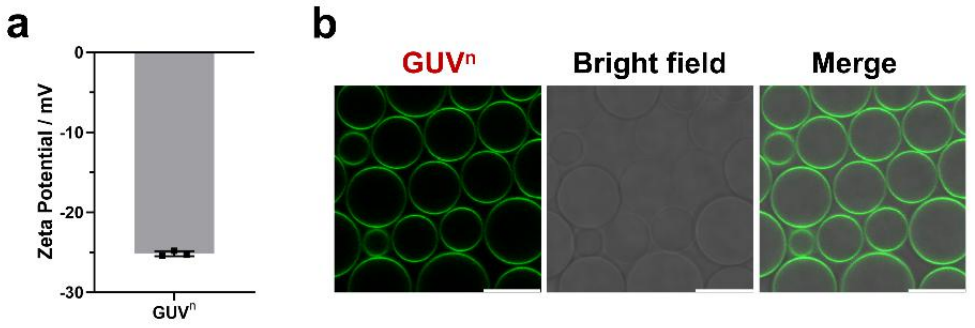

Figure S2. a) Zeta potentials of GUVⁿ-based protocell model. Data was presented as the mean value (n = 3). b) Confocal microscopy images of the protocell model GUVⁿ prepared via the electroformation method. Scale bar: 10 μm.

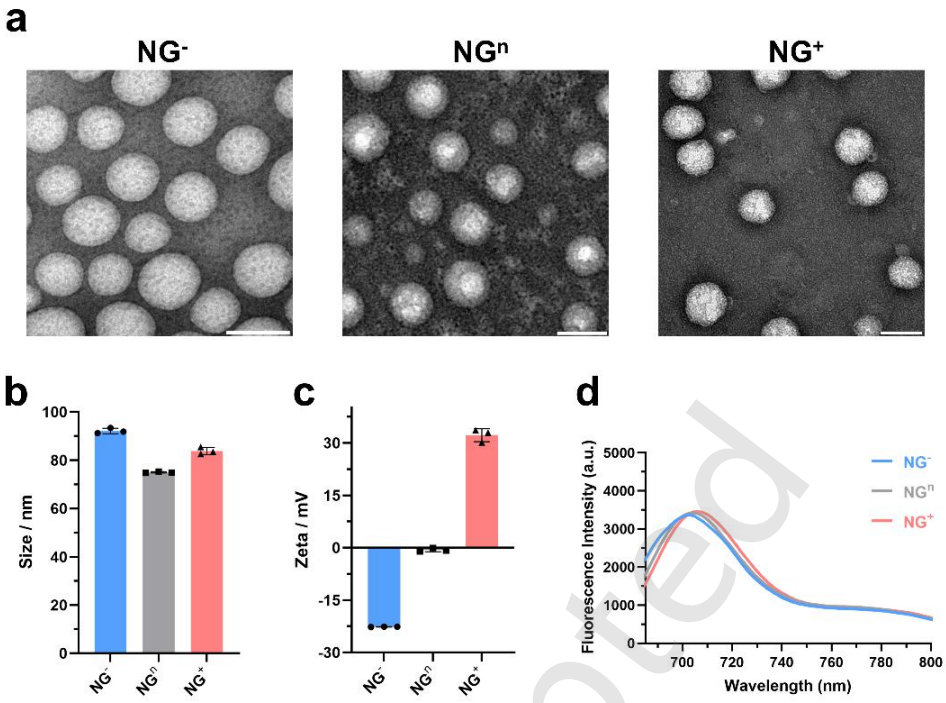

Figure S3. a) TEM images of charge gradient nanoparticles NG^-, NG^n, and NG^+, scale bar: 100 nm. b) The hydrodynamic diameter and c) zeta potentials of NGs. Data were presented as the mean ± standard deviation (SD, n = 3). d) Fluorescent intensity curve of the NGs with charge gradients, and with concentrations within the range of 60 ± 10 μg/mL; λex = 675 nm.

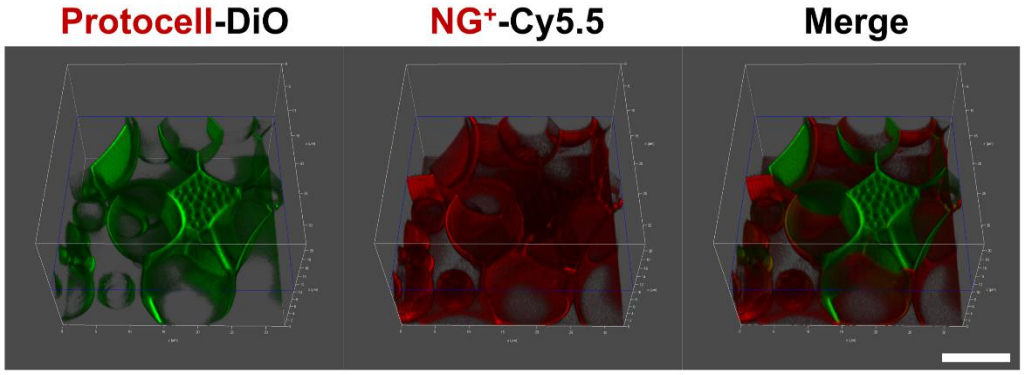

Figure S4. 3D reconstruction images of protocell co-incubated with NG^+ for 2 h. Scale bar: 10 μm.

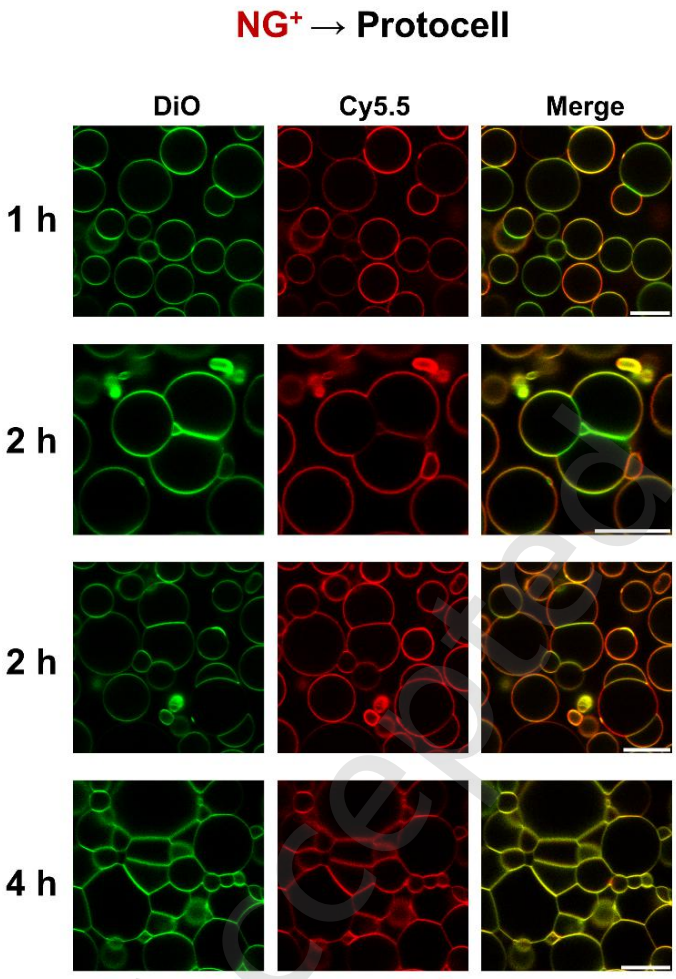

Figure S5. Confocal microscopy images of GUV^{n} co-incubated with NG^{+} for 1, 2, and 4 h, respectively, revealing progressive interaction patterns. Scale bar: 10 μm.

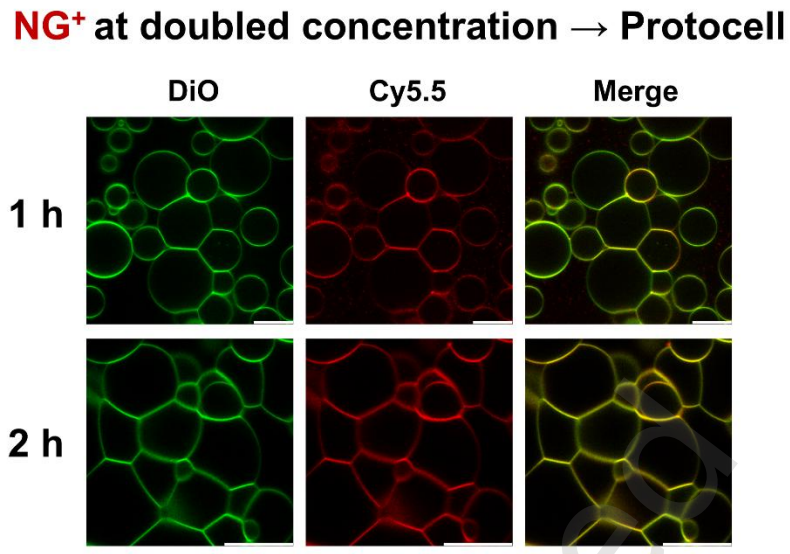

Figure S6. Confocal microscopy images of GUV^n co-incubated with doubled concentration of NG^+ for 1 h and 2 h, revealing more intensive and rapid interaction-induced protocell deformability. Scale bar: 10 μm.

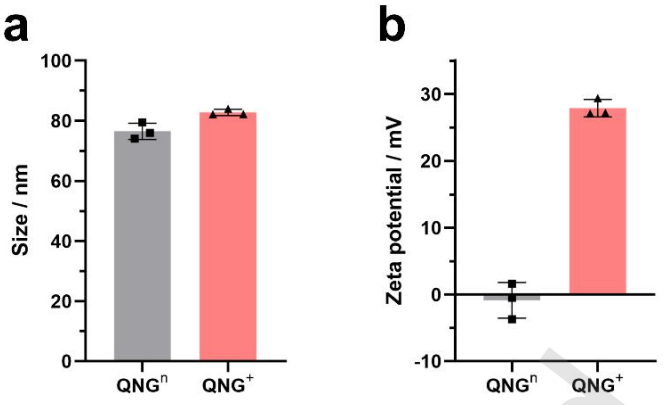

Figure S7. a) The hydrodynamic diameters and b) zeta potentials of charge gradient nanoparticles functionalized with the fluorescent quencher BHQ1: NG^n@BHQ1 and NG^+@BHQ1. Data were presented as the mean ± standard deviation (SD, n = 3).

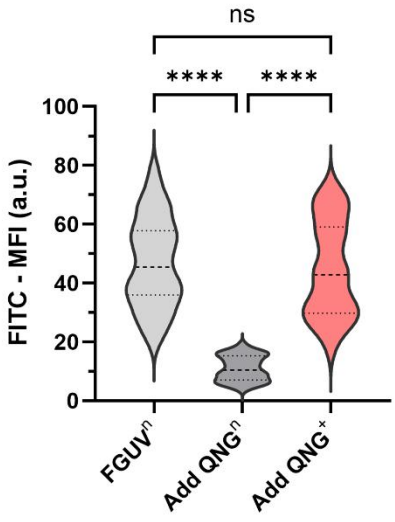

Figure S8. Statistical analysis of mean fluorescence intensity of FITC within $FGUV^n$ protocells before and after addition of QNG^n and QNG^+. Data were presented as violin plots displaying kernel density distributions, showing median (central dot) and interquartile range (inner whiskers), n = 30.

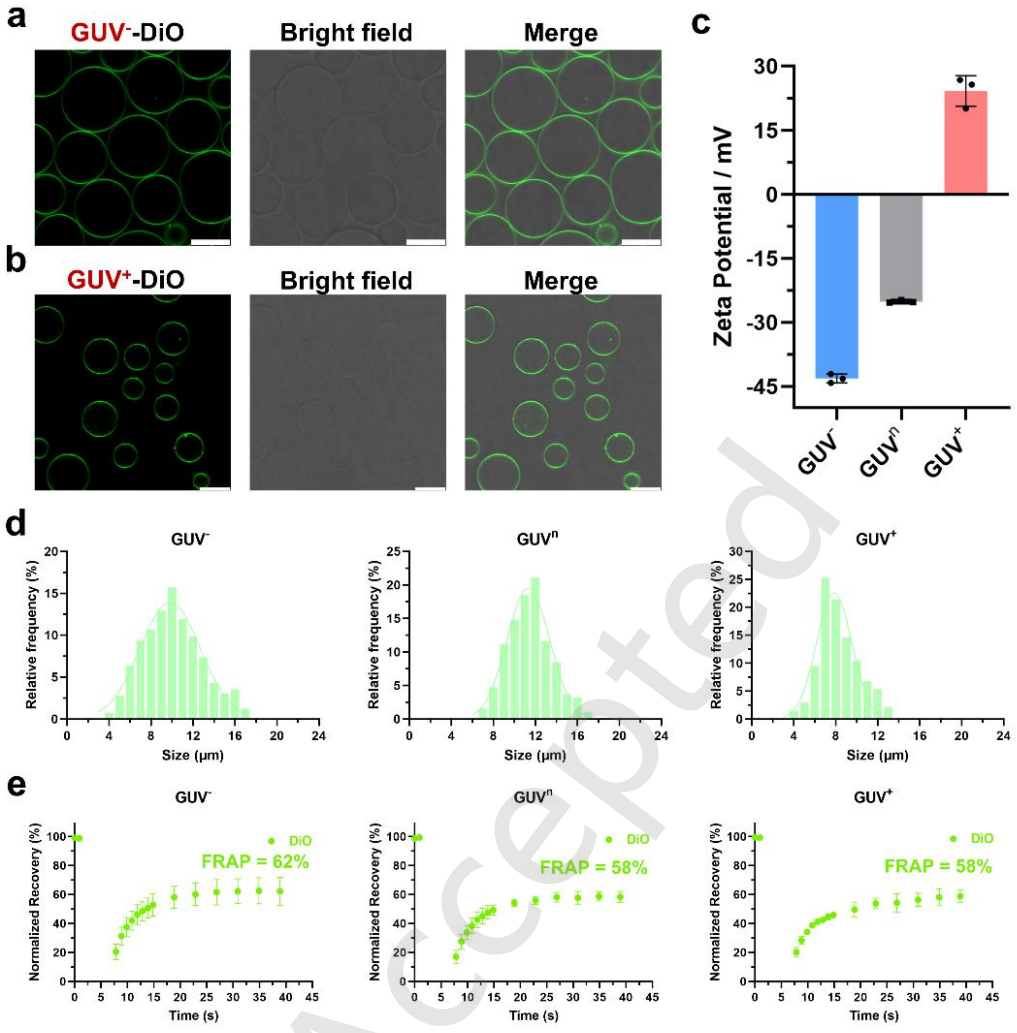

Figure S9. A series of fundamental characterizations of GUVs with different charges. Confocal microscopy images of a) GUV^- and b) GUV^+ constructed using the electroformation method and stained with DiO to visualize the phospholipid membrane. Scale bars: 10 μm. c) Zeta potentials of GUV^-, GUV^n, and GUV^+. Data were presented as the mean ± standard deviation (SD, n = 3). d) The diameters of GUV^-, GUV^n, and GUV^+ calculated from their respective Confocal microscopy images. e) FRAP data for DiO in the membranes of GUV^-, GUV^n, and GUV^+, with fluorescence recovery rates of 62 ± 5%, 58 ± 2%, and 58 ± 3%, respectively. Data are presented as the mean ± standard deviation (SD, n = 6).

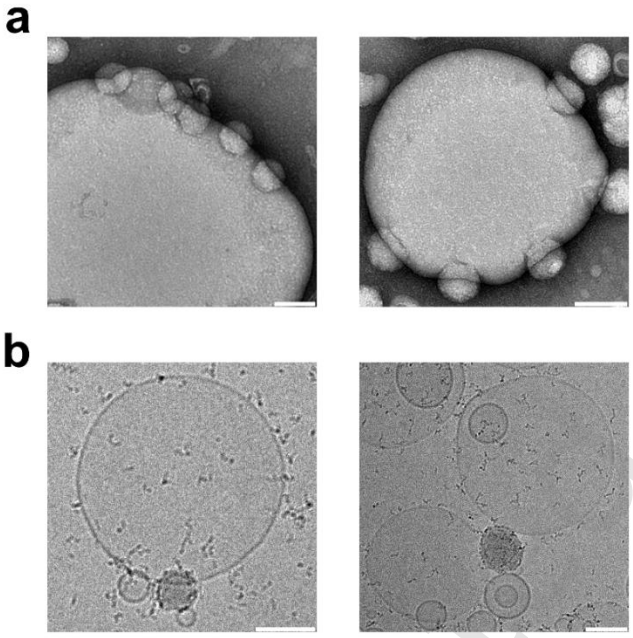

Figure S10. a) TEM images and b) Cryo-TEM images of nano-protocells co-incubated with NG^+. Scale bar: 100 nm.

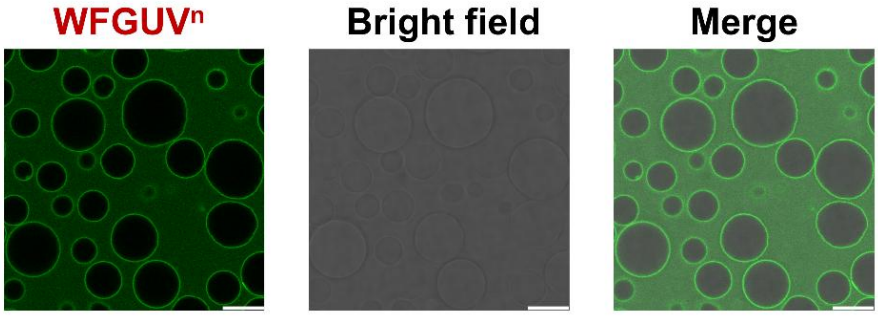

Figure S11. Confocal microscopy images of the protocell model WFGUV^n (externally loaded FITC-Dextran with a molecular weight of 4 kDa) prepared via the electroformation method. Scale bar: 10 μm.

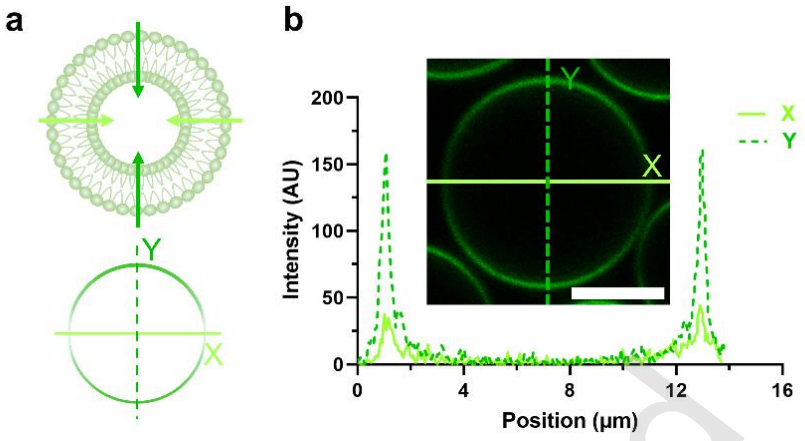

Figure S12. Angular dependence of the fluorescence of DiO on protocell membranes. a) Schematic illustration of the angular dependence of the fluorescence. b) Polarization effect exhibited as a strong angular dependence of the intensity of DiO along the protocell membrane, as emphasized with the line profiles along the respective solid or dashed lines indicated on the confocal microscopy image. The intensity line profiles were generated in the vertical and horizontal directions. Scale bars: 5 μm.

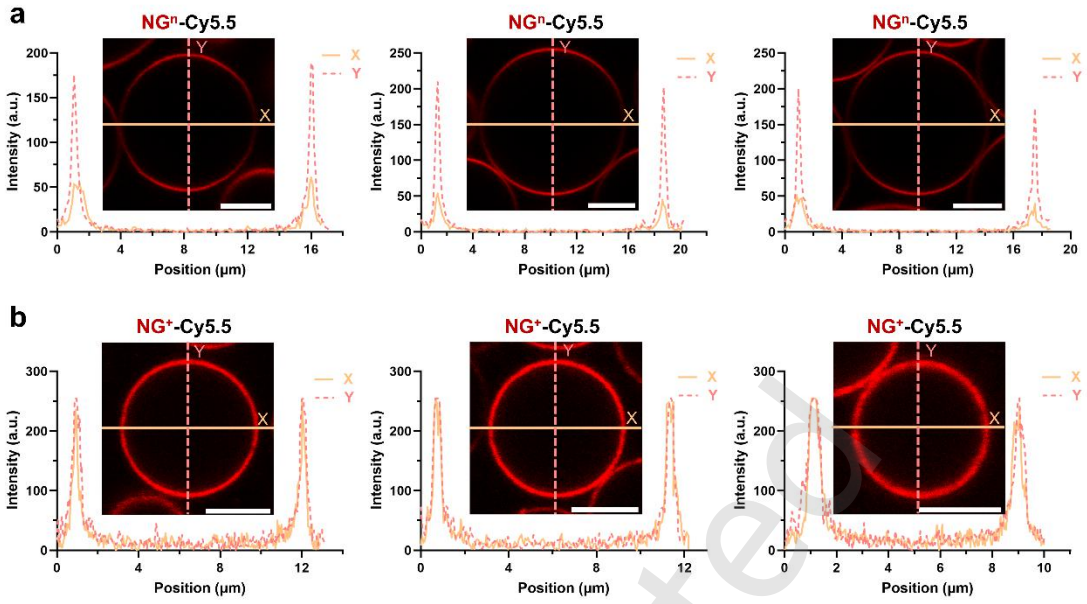

Figure S13. Angular dependence of fluorescence of the NGs functionalized with Cy5.5 on protocell membranes. a) Polarization effect exhibited as a strong angular dependence of the intensity of NG^n functionalized with Cy5.5 along the protocell membrane, as emphasized with the line profiles along the respective solid or dashed lines indicated on the Confocal microscopy image. b) No polarization effect was observed in the protocell membrane after co-incubation with NG^+ functionalized with Cy5.5. The intensity line profiles were generated in the vertical and horizontal directions. Scale bars: 5 μm.

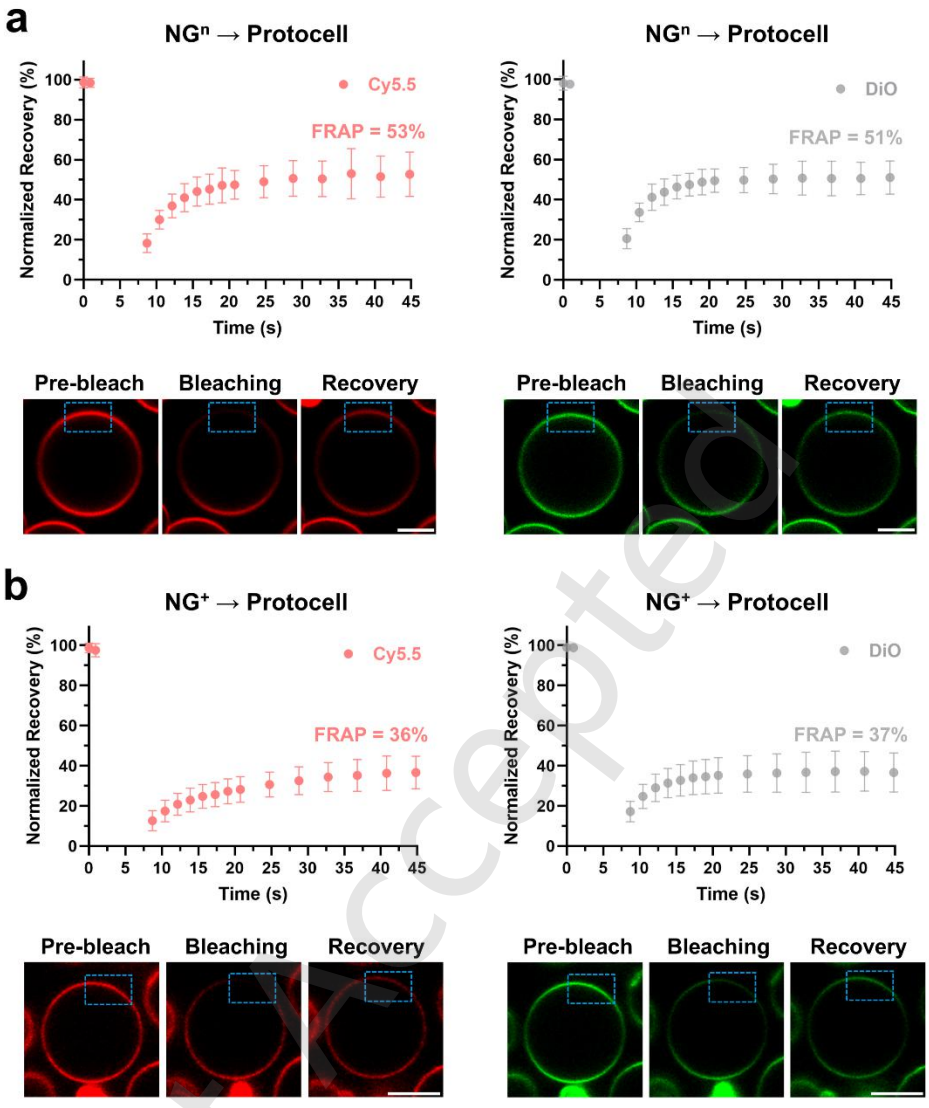

Figure S14. The fluidity properties of protocell phospholipid membranes and membrane-associated NGs were quantitatively assessed through the fluorescence recovery after photobleaching (FRAP) method. a) FRAP data for nanoparticle fluorescence Cy5.5 and membrane fluorescence DiO in the NG^{n}→Protocell group, with fluorescence recovery rates of 53±6% and 51±4%, respectively. b) FRAP data for nanoparticle fluorescence Cy5.5 and membrane fluorescence DiO in the NG^{+}→Protocell group, with fluorescence recovery rates of 36±3% and 37±4%, respectively. Data are presented as the mean ± standard deviation (SD, n = 10). Scale bar: 5 μm.

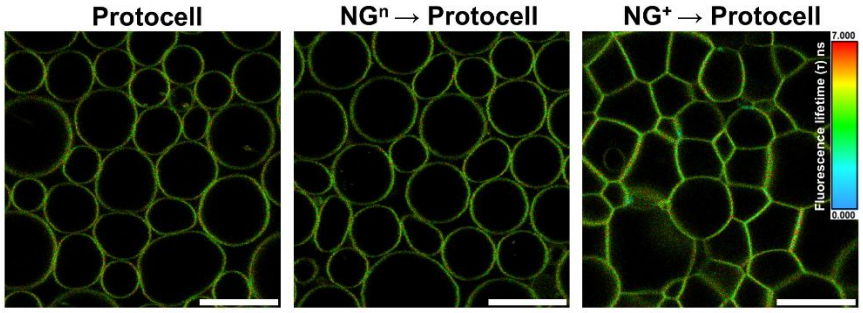

Figure S15. Fluorescence lifetime (τ) imaging of Flipper-TR probe in protocells before and after addition of NG^n and NG^+. Scale bar: 20 μm.

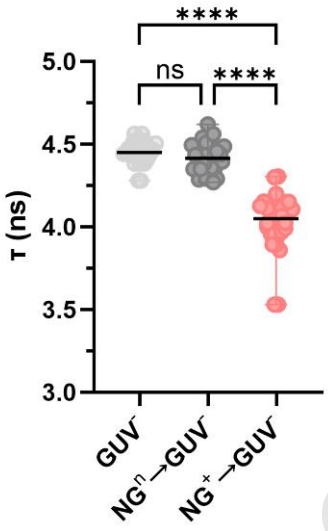

Figure S16. The fluorescence lifetimes of the phospholipid membranes in untreated GUV^- and GUV^- treated with NGs (NG^n and NG^+) were measured using a Flipper TR membrane tension probe. Statistical graph showing individual data points indicating fluorescence lifetime τ of 30 selected regions-of-interest (ROIs) across three biological replicates. Statistical analysis was performed via one-way analysis of variance ($n = 30$, *$p < 0.05$, **$p < 0.01$, ***$p < 0.001$, and ****$p < 0.0001$).

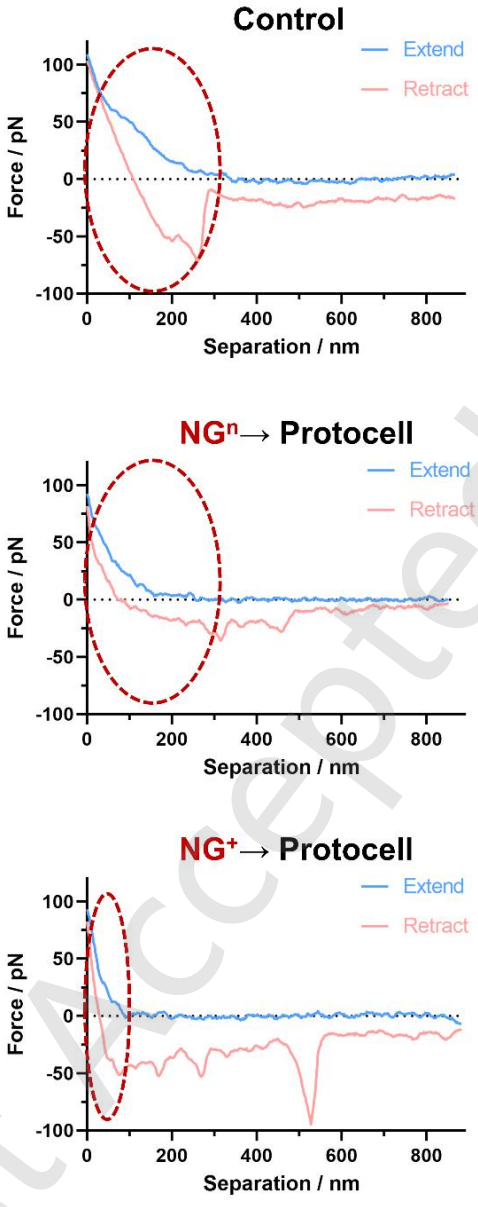

Figure S17. The mechanical force curves of untreated protocells and protocells treated with NGs (NG^n and NG^+) were obtained using Atomic Force Microscopy (AFM). The results obtained via AFM characterization were processed using NanoScope Analysis (Bruker) software, and the Young's modulus was calculated by fitting the data with the Hertzian model.

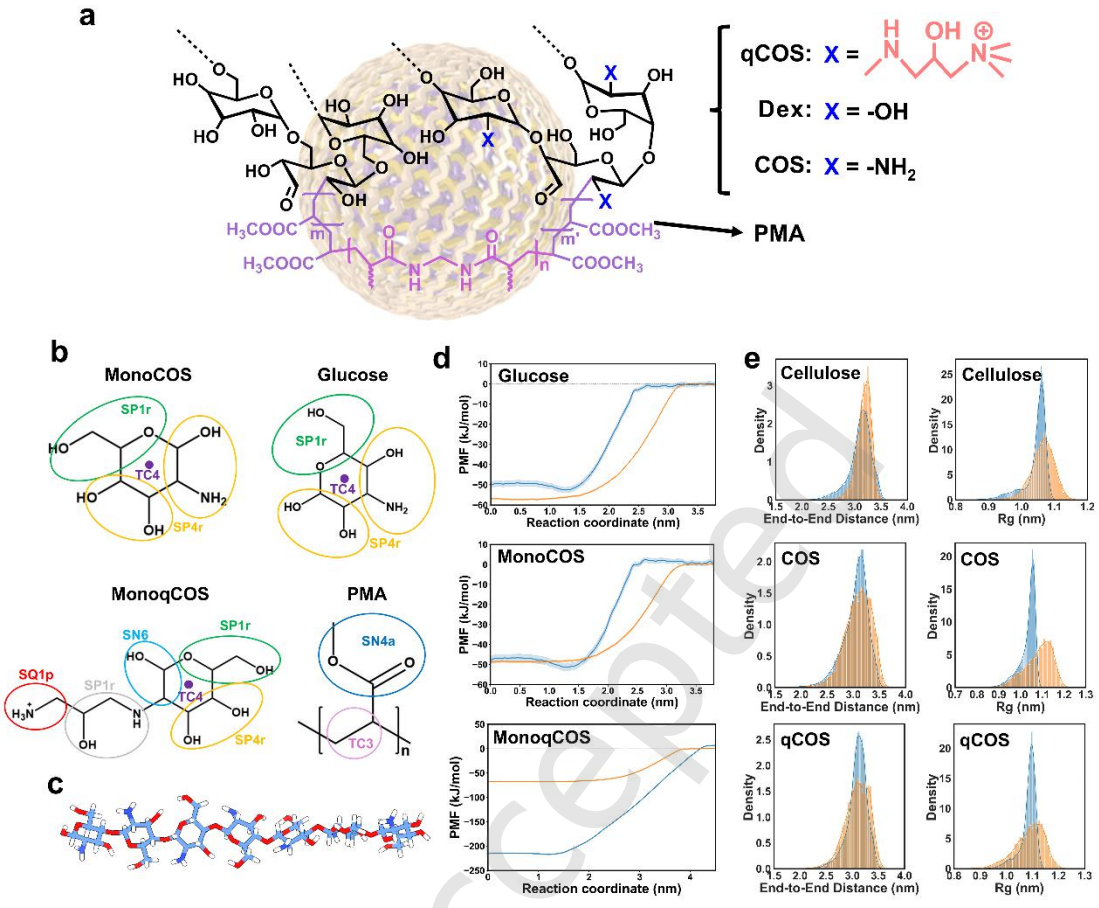

Figure S18. Coarse-grained model of the polymers. a) Chemical structure of the polymer constituting NG^{+} and NG^{n} nanoparticles. COS, qCOS, Dex and PMA refer to chitosan oligosaccharide, quaternized chitosan oligosaccharide, dextran and polymethyl acrylate, respectively. b) Mapping of the all-atom structures of monosaccharide units of COS (MonoCOS) and monosaccharide units of qCOS (MonoqCOS) to the coarse-grained model. c) Representative conformation of the heptasaccharide chains (COS is used as an example). d) Oil-water partition free energy profiles at the coarse-grained (orange line) and all-atom (blue line) levels for glucose, monoCOS and monoqCOS. e) End-to-end distance (left panel) and radius of gyration (R_g, right panel) of the three heptasaccharide chains (glucose, monoCOS and monoqCOS) in coarse-grained and all-atom simulations.

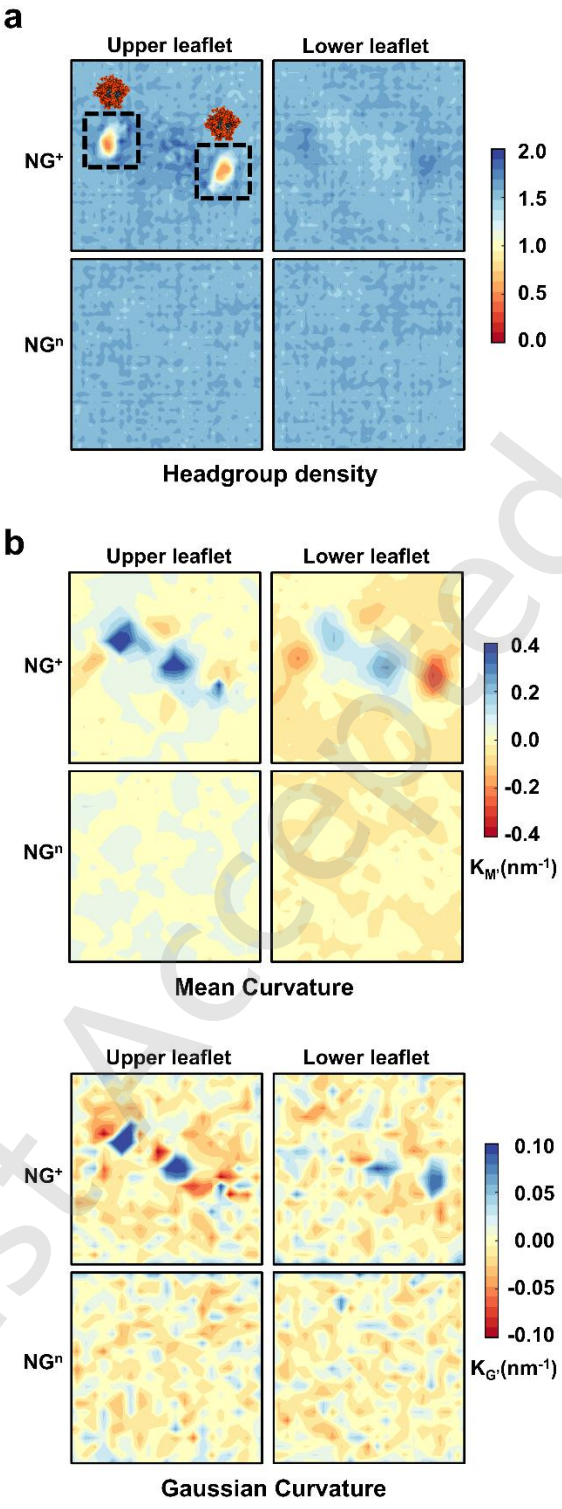

Figure S19. a) Two-dimensional density maps of lipid headgroups in NG^+ and NG^n simulations for the upper and lower leaflets. The color scale represents the local number density, which is defined as the average count of headgroup beads per grid cell. Color gradients indicate local number density from depletion (red) to enrichment (blue). b) The mean and Gaussian curvatures of the membranes in NG^+ and NG^n simulations. Results of the two leaflets are both shown.

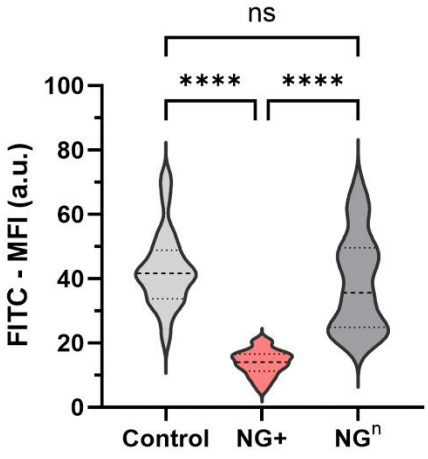

Figure S20. Statistical analysis of mean fluorescence intensity of FITC within FGUV^n protocells following 1 h interaction between NGs and binary protocell populations. Data were presented as violin plots displaying kernel density distributions, showing median (central dot) and interquartile range (inner whiskers), n = 30.

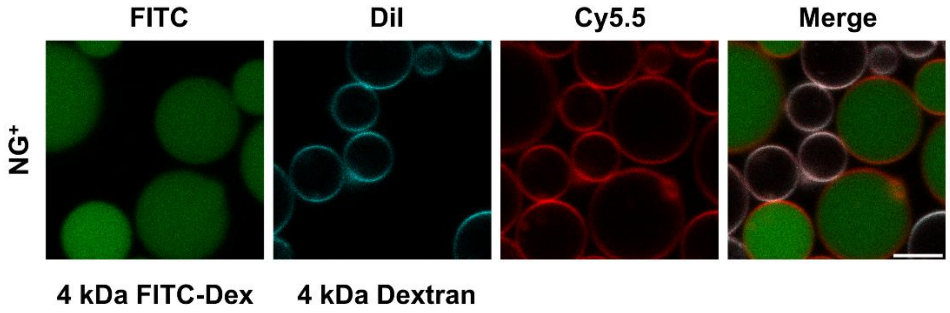

Figure S21. Confocal microscopy images of binary protocell populations interact with NG^+ for 1 h, with FITC-labeled $FGUV^n$ protocells internally loaded with 4 kDa FITC-Dex and DiI-labeled GUV^n protocells internally loaded with the same concentration of 4 kDa Dextran. Scale bars: 10 μm.

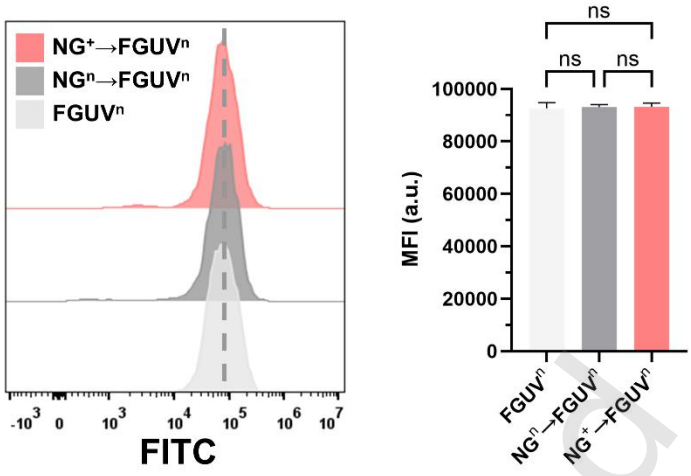

Figure S22. Flow cytometry data and quantified analysis of MFI for $FGUV^n$ co-incubated with NG^n and NG^+ for 2 h.

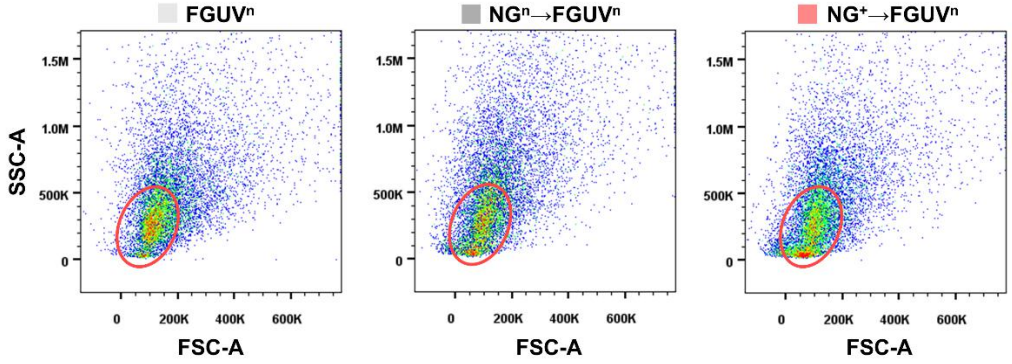

Figure S23. Flow cytometry data of SSC-A and FSC-A channels for $FGUV^n$ before and after addition of NG^n and NG^+.

3. Supplementary table

Table S1. List of sample abbreviations.

Abbreviation	Sample name	Abbreviation	Sample name
NGs	Nanogels	GUV	Giant unilamellar vesicles
Dex	Dextran	POPC	1-Palmitoyl-2-oleoyl-sn-glycero-3-PC
COS	Chitosan oligosaccharide	DOTAP	Dioleoyl-3-trimethylammonium propane
CAN	Ceric ammonium nitrate	DOPA	1,2-Dioleoyl-sn-glycero-3-phosphate
MA	Methyl acrylate	DiO	3,3'-Dioctadecyloxacarbo-cyanineperchlorate
PMA	Polymethyl acrylate	DiI	1,1'-Dioctadecyl-3,3,3',3'-tetramethylindo-carbocyanine perchlorate
MBA	*N*,*N*-methylene-bis-acrylamide	DPH	1,6-Diphenyl-1,3,5-hexatriene
GTMAC	Glycidyltrimethylammonium Chloride	GUV^n	Conventional GUV with POPC as phospholipid component
DMAP	4-Dimethyl-aminopyridine	GUV^-	Negatively charged GUV incorporating the anionic lipid DOPA
SA	Succinic anhydride	GUV^+	Positively charged GUV incorporating the cationic lipid DOTAP
qCOS	Quaternized chitosan Oligosaccharides	FGUV	GUV internally loaded with FITC-Dextran
NG^+	Positively charged glycan nanogels	WFGUV	GUV externally loaded with FITC-Dextran
NG^-	Negatively charged glycan nanogels	BGUV	GUV internally loaded with quencher BHQ1
NG^n	Uncharged glycan nanogels	PMF	Potential of mean force
Cy5.5	Cyanine 5.5	MWCO	Molecular Weight Cut Off
QNG	Quencher NG	ROI	Regions of interest
FITC	Fluorescein Isothiocyanate	GISA	Graft copolymerization-induced self-assembly
DMSO	Dimethyl sulfoxide	FRAP	Fluorescence recovery after photobleaching

4. Supplementary References

[1] Cheng, M.; Liu, L.; Zhang, P.; Xiong, S.; Dou, H. Cell Coding Arrays Based on Fluorescent Glycan Nanoparticles for Cell Line Identification and Cell Contamination Evaluation. *ACS Appl. Mater. Inter.* **2021**, *13*, 44054-44064.

[2] Wang, C.; Guan, W.; Peng, J.; Chen, Y.; Xu, G.; Dou, H. Gene/paclitaxel co-delivering nanocarriers prepared by framework-induced self-assembly for the inhibition of highly drug-resistant tumors. *Acta Biomater.* **2020**, *103*, 247-258.

[3] Wang, H.; Dai, T.; Li, S.; Zhou, S.; Yuan, X.; You, J.; Wang, C.; Mukwaya, V.; Zhou, G.; Liu, G.; Wei, X.; Dou, H. Scalable and cleavable polysaccharide nanocarriers for the delivery of chemotherapy drugs. *Acta Biomater.* **2018**, *72*, 206-216.

[4] Liang, Y.; Li, Z.; Huang, Y.; Yu, R.; Guo, B. Dual-Dynamic-Bond Cross-Linked Antibacterial Adhesive Hydrogel Sealants with On-Demand Removability for Post-Wound-Closure and Infected Wound Healing. *ACS Nano* **2021**, *15*, 7078-7093.

[5] Zhao, X.; Guo, B.; Wu, H.; Liang, Y.; Ma, P. X. Injectable antibacterial conductive nanocomposite cryogels with rapid shape recovery for noncompressible hemorrhage and wound healing. *Nat. Commun.* **2018**, *9*, 2784.

[6] Montes, L.-R.; Ahyayauch, H.; Ibarguren, M.; Sot, J.; Alonso, A.; Bagatolli, L. A.; Goni, F. M. *Electroformation of Giant Unilamellar Vesicles from Native Membranes and Organic Lipid Mixtures for the Study of Lipid Domains under Physiological Ionic-Strength Conditions*, 2010.

[7] Zhang, X.; Li, C.; Liu, F.; Mu, W.; Ren, Y.; Yang, B.; Han, X. High-throughput production of functional prototissues capable of producing NO for vasodilation. *Nat. Commun.* **2022**, *13*, 29571.

[8] Zong, W.; Ma, S.; Zhang, X.; Wang, X.; Li, Q.; Han, X. A Fissionable Artificial Eukaryote-like Cell Model. *J. Am. Chem. Soc.* **2017**, *139*, 9955-9960.

[9] Large, D. E.; Abdelmessih, R. G.; Fink, E. A.; Auguste, D. T. Liposome composition in drug delivery design, synthesis, characterization, and clinical application. *Adv. Drug Del. Rev.* **2021**, *176*, 113851.

[10] Needham, D.; McIntosh, T. J.; Evans, E. Thermomechanical and transition properties of dimyristoylphosphatidylcholine/cholesterol bilayers. *Biochemistry* **1988**, *27*, 4668-4673.

[11] Lv, Y.; Xu, C.; Zhao, X.; Lin, C.; Yang, X.; Xin, X.; Zhang, L.; Qn, C.; Han, X.; Yang, L.; He, W.; Yin, L. Nanoplatform Assembled from a CD44-Targeted Prodrug and Smart Liposomes for Dual Targeting of Tumor Microenvironment and Cancer Cells. *ACS Nano* **2018**, *12*, 1519-1536.

[12] Cai, C. X.; Zhu, H.; Chen, J. W. Overexpression of caveolin-1 increases plasma membrane fluidity and reduces P-glycoprotein function in Hs578T/Dox. *Biochem. Bioph. Res. Co.* **2004**, *320*, 868-874.

[13] Governa, M.; Valentino, M.; Visona, I.; Rocco, M. Impairment of Human Polymorphonuclear Leukocyte Chemotaxis by 2.5-Hexanedione. *Cell Biol. Toxicol.* **1986**, *2*, 33-39.

[14] Souza, P. C. T.; Alessandri, R.; Barnoud, J.; Thallmair, S.; Faustino, I.; Grünewald, F.; Patmanidis, I.; Abdizadeh, H.; Bruininks, B. M. H.; Wassenaar, T. A.; Kroon, P. C.; Melcr, J.; Nieto, V.; Corradi, V.; Khan, H. M.; Domański, J.; Javanainen, M.; Martinez-Seara, H.; Reuter, N.; Best, R. B.; Vattulainen, I.; Monticelli, L.; Periole, X.; Tieleman, D. P.; de Vries, A. H.; Marrink, S. J. Martini 3: a general purpose force field for coarse-grained molecular dynamics. *Nat. Methods* **2021**, *18*, 382-388.

[15] Grünewald, F.; Alessandri, R.; Kroon, P. C.; Monticelli, L.; Souza, P. C. T.; Marrink, S. J. Polyply; a python suite for facilitating simulations of macromolecules and nanomaterials. *Nat. Commun.* **2022**, *13*, 68.

[16] Grünewald, F.; Punt, M. H.; Jefferys, E. E.; Vainikka, P. A.; König, M.; Virtanen, V.; Meyer, T. A.; Pezeshkian, W.; Gormley, A. J.; Karonen, M.; Sansom, M. S. P.; Souza, P. C. T.; Marrink, S. J. Martini 3 Coarse-Grained Force Field for Carbohydrates. *J. Chem. Theory Comput.* **2022**, *18*, 7555-7569.

[17] Kästner, J. Umbrella sampling. *WIREs: Comp. Mol. Sci.* **2011**, *1*, 932-942.

[18] Guvench, O.; Hatcher, E. R.; Venable, R. M.; Pastor, R. W.; MacKerell Jr., A. D. Additive Empirical CHARMM Force Field for glycosyl linked hexopyranoses. *J. Chem. Theory Comput.* **2009**, *5*, 2353-2370.

[19] Vanommeslaeghe, K.; MacKerell, A. D., Jr. Automation of the CHARMM General Force Field (CGenFF) I: Bond Perception and Atom Typing. *J. Chem. Inf. Model.* **2012**, *52*, 3144-3154.

[20] Vanommeslaeghe, K.; Raman, E. P.; MacKerell, A. D., Jr. Automation of the CHARMM General Force Field (CGenFF) II: Assignment of Bonded Parameters and Partial Atomic Charges. *J. Chem. Inf. Model.* **2012**, *52*, 3155-3168.

[21] Guvench, O.; Mallajosyula, S. S.; Raman, E. P.; Hatcher, E.; Vanommeslaeghe, K.; Foster, T. J.; Jamison, F. W., II; MacKerell, A. D., Jr. CHARMM Additive All-Atom Force Field for Carbohydrate Derivatives and Its Utility in Polysaccharide and Carbohydrate–Protein Modeling. *J. Chem. Theory Comput.* **2011**, *7*, 3162-3180.

[22] Raman, E. P.; Guvench, O.; MacKerell, A. D., Jr. CHARMM Additive All-Atom Force Field for Glycosidic Linkages in Carbohydrates Involving Furanoses. *J. Phys. Chem. B* **2010**, *114*, 12981-12994.

[23] Vanommeslaeghe, K.; Hatcher, E.; Acharya, C.; Kundu, S.; Zhong, S.; Shim, J.; Darian, E.; Guvench, O.; Lopes, P.; Vorobyov, I.; Mackerell Jr, A. D. CHARMM general force field: A force field for drug-like molecules compatible with the CHARMM all-atom additive biological force fields. *J. Comput. Chem.* **2010**, *31*, 671-690.

[24] Jo, S.; Kim, T.; Iyer, V. G.; Im, W. CHARMM-GUI: A web-based graphical user interface for CHARMM. *J. Comput. Chem.* **2008**, *29*, 1859-1865.

[25] Bussi, G.; Donadio, D.; Parrinello, M. Canonical sampling through velocity rescaling. *J. Chem. Phys.* **2007**, *126*.

[26] Nosé, S.; Klein, M. L. Constant pressure molecular dynamics for molecular systems. *Mol. Phys.* **1983**, *50*, 1055-1076.

[27] Parrinello, M.; Rahman, A. Polymorphic transitions in single crystals: A new molecular dynamics method. *J. Appl. Phys.* **1981**, *52*, 7182-7190.

[28] Tironi, I. G.; Sperb, R.; Smith, P. E.; van Gunsteren, W. F. A generalized reaction field method for molecular dynamics simulations. *J. Chem. Phys.* **1995**, *102*, 5451-5459.

[29] Hess, B.; Bekker, H.; Berendsen, H. J. C.; Fraaije, J. G. E. M. LINCS: A linear constraint solver for molecular simulations. *J. Comput. Chem.* **1997**, *18*, 1463-1472.

[30] Bernetti, M.; Bussi, G. Pressure control using stochastic cell rescaling. *J. Chem. Phys.* **2020**, *153*.

[31] Darden, T.; York, D.; Pedersen, L. Particle mesh Ewald: An N·log(N) method for Ewald sums in large systems. *J. Chem. Phys.* **1993**, *98*, 10089-10092.

[32] Essmann, U.; Perera, L.; Berkowitz, M. L.; Darden, T.; Lee, H.; Pedersen, L. G. A smooth particle mesh Ewald method. *J. Chem. Phys.* **1995**, *103*, 8577-8593.

[33] Hub, J. S.; de Groot, B. L.; van der Spoel, D. g_wham—A Free Weighted Histogram Analysis Implementation Including Robust Error and Autocorrelation Estimates. *J. Chem. Theory Comput.* **2010**, *6*, 3713-3720.

[34] Martínez, L.; Andrade, R.; Birgin, E. G.; Martínez, J. M. PACKMOL: A package for building initial configurations for molecular dynamics simulations. *J. Comput. Chem.* **2009**, *30*, 2157-2164.

[35] Gowers, R. J.; Linke, M.; Barnoud, J.; Reddy, T.; Melo, M. N.; Seyler, S. L.; Domanski, J. J.; Dotson, D. L.; Buchoux, S.; Kenney, I. M.; Beckstein, O. MDAnalysis: A Python Package for the Rapid Analysis of Molecular Dynamics Simulations. In *SciPy*, 2016.

[36] Michaud-Agrawal, N.; Denning, E. J.; Woolf, T. B.; Beckstein, O. MDAnalysis: A toolkit for the analysis of molecular dynamics simulations. *J. Comput. Chem.* **2011**, *32*, 2319-2327.